

# **Interannual variability of the Australian summer monsoon sustained through internal processes: wind-evaporation feedback, dynamical air-sea interaction and soil moisture memory**

Shion Sekizawa,<sup>a</sup> Hisashi Nakamura,<sup>a</sup> Yu Kosaka.<sup>a</sup>

<sup>a</sup> *Research Center for Advanced Science and Technology, the University of Tokyo, Tokyo, Japan*

(Corresponding author: Shion Sekizawa, RCAST, the University of Tokyo, Japan.  
E-mail: shion@atmos.rcast.u-tokyo.ac.jp)

\* This manuscript has been submitted for publication in *Journal of Climate*. It is not yet peer-reviewed. Subsequent versions of this manuscript may have slightly different content. If accepted, the final version of this manuscript will be available via a link on this webpage.

## **ABSTRACT**

In northern Australia (NAUS), mean rainfall during the Australian summer monsoon (AUSM) season exhibits distinct interannual variability despite weak influence from tropical sea surface temperature (SST) variability. The present study investigates mechanisms for the strong and persistent rainfall anomalies throughout the AUSM season. When the AUSM is stronger than normal, the low-level monsoonal circulation intensifies in response to the stronger convective activity over NAUS. The intensified surface westerlies over the tropical southeastern Indian Ocean (SEIO) enhance oceanic evaporation locally and downstream moisture transport into NAUS. This wind-evaporation feedback is verified through a moist static energy budget analysis. For this feedback to work effectively, SST cooling due to the stronger AUSM should be weak enough not to suppress the oceanic evaporation in the tropical SEIO. Our mixed-layer heat budget analysis based on an ocean model hindcast experiment reveals that anomalous downwelling in the subsurface SEIO, which is induced dynamically by the intensified monsoon westerlies, partially offsets the SST cooling. The land-surface evaporation over the continental inland area is also enhanced significantly in the middle and later portions of the monsoon season associated with increased soil moisture, suggesting its memory effect for the persistence of rainfall anomalies. The AUSM variability can therefore be regarded as a self-sustaining internal variability in the atmosphere-ocean-land surface coupled system, rather than just an atmospheric internal variability.

## **SIGNIFICANCE STATEMENT**

We aim to understand why summer monsoon rainfall in northern Australia varies markedly from one year to another even under the weak influence of large-scale sea surface temperature fluctuations, such as El Niño/La Niña. Our analyses based mainly on observational datasets reveal that wind-induced changes in oceanic evaporation south of Java significantly modulates the water vapor transport into northern Australia. We also find that ocean dynamics helps this wind-evaporation feedback process and continental soil moisture may act to prolong anomalous rainfall by its memory effect. This study shows the self-sustaining nature of the Australian summer monsoon variability under the atmosphere-ocean-land surface interactions, which deepens our understandings of the monsoon system.

## **1. Introduction**

In austral summer, active convection around the Maritime Continent is concentrated in northern Australia (NAUS) in accordance with the southward migration of intense solar radiation into the Southern Hemisphere (Meehl 1987; Mitchell and Wallace 1992). Under the strong insolation, enhanced land-sea thermal contrast forces low-level cyclonic (monsoonal) circulation, and associated moisture supply from the tropical southeastern Indian Ocean (SEIO) intensifies convective activity over NAUS, driving the Australian summer monsoon (AUSM; Suppiah 1992; Kawamura et al. 2002). The AUSM typically onsets in late December along with the establishment of monsoon westerlies and then withdraws in early March (Holland 1986; Hendon and Liebmann 1990a; Drosowsky 1996; Kajikawa et al. 2010; Evans et al. 2014). It forms the core period of the NAUS rainfall season, in which the land surface holds enough water for vegetation to grow (Lo et al. 2007). Since most of the annual rainfall in NAUS is brought about by the AUSM, the understanding, prediction and projection of AUSM rainfall variability are important for the agriculture and livestock industry in Australia (Mollah and Cook 1996; Bowman 2002; Howden et al. 2008). In addition, the AUSM variability remotely affects the climate in other regions of the globe. For instance, the anomalous AUSM modulates the strength of the East Asian winter monsoon, causing significant anomalies of temperature and precipitation over East Asia and the western North Pacific (Sekizawa et al. 2021).

Many studies have investigated links of the AUSM with tropical sea surface temperature (SST) variability, which is one of the major sources of seasonal predictability. It is known that La Niña leads to earlier onset of the AUSM than El Niño, while the phase of El Niño-Southern Oscillation (ENSO) does not significantly affect the retreat date (Holland 1986; Drosowsky 1996; Kajikawa et al. 2010; Evans et al. 2014). The seasonal-mean rainfall in summer has also weaker correlation with ENSO than that in spring (Drosowsky and Williams 1991; Risbey et al. 2009). Wu and Kirtman (2007) and Taschetto et al. (2011) emphasized the importance of SST anomalies in the Indian Ocean rather than those in the Pacific. These facts imply a seasonal weakening of the ENSO-AUSM linkage from austral spring to summer despite ENSO events typically maturing in summer (Larkin and Harrison 2002). Hendon et al. (2012) pointed out that seasonal predictability for NAUS rainfall decreases from spring to summer in association with the establishment of monsoon westerlies over the tropical SEIO. Under the prevailing trade easterlies in spring, enhanced NAUS convection can be supported through wind-evaporation-SST feedback (Xie and Philander 1994), where anomalous surface westerlies over the SEIO forced by the enhanced convection weaken the trade winds and thus reduce oceanic evaporation and mixing, acting to increase SST. By contrast, under the monsoonal westerlies in summer, anomalous westerlies instead intensify the surface winds, thus acting to lower SST. Thus, the atmosphere tends to influence the ocean (negative feedback) in summer rather than the other way round (positive feedback), suggesting that the anomalous NAUS convection is unlikely to be maintained by SST anomalies. Wu and Kirtman (2007) also found that their numerical experiment without coupling with the Indian Ocean weakens the ENSO-AUSM linkage, but not the total AUSM variability, suggesting the predominance of atmospheric internal variability.

It has been extensively documented that NAUS rainfall varies on intraseasonal timescales under the influence of atmospheric internal perturbations, such as the Madden-Julian Oscillation (MJO) and midlatitude synoptic eddies (e.g., Hendon and Liebmann 1990b; Wheeler et al. 2009; Berry et al. 2011; Narsey et al. 2017). On interannual timescales, however, fundamental properties and mechanisms of the internal variability of the summer NAUS rainfall had been overlooked until recently. Sekizawa et al. (2018) revealed that January–

February (JF)-mean NAUS rainfall anomalies are not a manifestation of modulated MJO events but that of the persistent rainfall anomalies throughout the AUSM season. They proposed that the AUSM variability can be sustained through a wind-evaporation feedback mechanism, where the intensified (weakened) monsoon westerlies due to enhanced (suppressed) NAUS convection act to enhance (suppress) the oceanic evaporation over the tropical SEIO and moisture transport into NAUS. This feedback mechanism works if SEIO SST cooling induced by the strong AUSM is weak enough to prevent the oceanic evaporation from being reduced. Their results thus suggest that summertime NAUS rainfall can vary interannually without being influenced by SST anomalies locally and remotely, as a manifestation of its dominant variability intrinsic to the AUSM system. They also found that warm anomalies emerge below the mixed layer in the SEIO under the stronger AUSM, suggesting that the subsurface warm anomalies may play a role in damping the SST cooling. This effect has, however, remained to be verified quantitatively.

In addition to the wind-evaporation feedback mechanism, atmosphere-land surface interactions can also influence the AUSM rainfall variability. Sharmila and Hendon (2020) argued that positive feedback between anomalous soil moisture and rainfall through land-surface evaporation can sustain these anomalies over NAUS, especially on decadal-to-multidecadal timescales. Martius et al. (2021) also examined atmospheric responses to anomalous soil moisture in Australia through a set of numerical model experiments, to show that NAUS rainfall increases as a response to the anomalously wet land surface.

The aim of the present study is to deepen our understandings of the internal variability dominated in the AUSM system. Here, we verify that the wind-evaporation-convection feedback sustains the anomalous AUSM activity, in demonstrating that the wind-induced anomalous evaporation in the tropical SEIO is an essential source of anomalous moist static energy (MSE). We further quantitatively evaluate the damping effect of subsurface anomalies in the tropical SEIO on the SST anomalies, while investigating the effect of soil moisture for the persistency of the anomalous AUSM rainfall. Through these analyses, we attempt to reveal the nature of self-sustaining AUSM variability in the atmosphere-ocean-land surface coupled system, rather than just an atmospheric internal variability.

This paper is structured as follows. Section 2 describes datasets and analysis methods used in this study. In section 3, we examine the relationship between NAUS rainfall and tropical SST variability to confirm the domination of internal variability in the AUSM rainfall. Section 4 investigates mechanisms of persistent anomalous moisture supply into the convection anomalies over NAUS. The importance of wind-induced oceanic evaporation on sustaining the anomalous convection is verified through an MSE budget analysis, followed by a discussion on the potential role of soil moisture and land-surface evaporation. Section 5 assesses the role of dynamical air-sea interaction through a mixed-layer heat budget analysis based on a hindcast experiment with a high-resolution ocean general circulation model (OGCM). We provide a summary and discussion in section 6.

## **2. Data and methods**

### *a. Observational data*

In this study, we use the Australian Water Availability Project (AWAP) dataset obtained from the Australian Bureau of Meteorology. This is  $0.05^\circ \times 0.05^\circ$  gridded rainfall data over

continental Australia produced by interpolating station observations (Jones et al. 2009). To define an AUSM index (Fig. 1b), JF rainfall is averaged over the NAUS region [10°S–25°S, 120°E–145°E] (rectangular domain shown in Fig. 1a) every year for the period 1958–2021. Shading in Fig. 1a illustrates JF-mean rainfall anomalies regressed linearly onto the AUSM index for 1958–2021. Significant rainfall anomalies cover the entire NAUS and extend to its south in the middle of the continent, while rainfall anomalies in Western Australia and along the Pacific coast are insignificant. We also utilize evapotranspiration and soil moisture analyses for 1958–2019 from the Australian Water Resources Assessment system’s landscape model (AWRA-L), which is a water balance model with horizontal resolution of  $0.05^\circ \times 0.05^\circ$  driven by observed meteorological parameters (Frost et al. 2018). The soil moisture data is provided separately for three layers; upper (0–0.1 m), lower (0.1–1 m) and deeper (1–6 m) layers, and we integrate them over the three layers for our analyses. For many other meteorological variables, we use the Japanese 55-year Reanalysis (JRA-55) of the global atmosphere provided by the Japan Meteorological Agency (Kobayashi et al. 2015) with horizontal resolution of  $1.25^\circ \times 1.25^\circ$  and 37 isobaric levels, which is available from 1958. For comparison with JRA-55, ERA5 global reanalysis data (Hersbach et al. 2020) produced by the European Centre for Medium-Range Weather Forecasts (ECMWF) with horizontal resolution of  $1^\circ \times 1^\circ$  and 37 isobaric levels for 1980–2021 is also used in our MSE budget analysis.

Hadley Centre Sea Ice and SST (HadISST) with resolution of  $1^\circ \times 1^\circ$  (Rayner et al. 2003) is used for SST. This dataset is used for calculating the conventional tropical SST indices: Niño-3, Niño-3.4, Niño-4, El Niño Modoki index (EMI; Ashok et al. 2007) and Indian Ocean dipole mode index (DMI; Saji et al. 1999), all of which are based on regionally averaged SST (see Fig. S1 for their definitions). We also use Ocean Reanalysis System 5 (ORA-S5) from the ECMWF with horizontal resolution of  $1^\circ \times 1^\circ$  and 28 vertical levels within the upper 150 m (Zuo et al. 2019) for ocean temperature and currents. ORA-S5 provides five ensemble members with additional perturbations in forcing, observations and initial conditions. The ensemble mean fields are used in our analyses, but results are unchanged qualitatively if we use the individual ensemble members.

The basic statistical methods in this study are correlation and regression analyses with the AUSM index. A linear trend for the analysis period has been locally removed from any variables beforehand. The regressed anomalies are scaled to a unit standard deviation of the AUSM index to represent typical anomalies in a strong AUSM year. We consider that any asymmetries between strong and weak AUSM years are second-order features of the AUSM variability, and therefore they are not discussed in this study. Thus, typical anomalies in a weak AUSM year are assumed to be a mirror image of those in a strong year. Statistical significance of the correlation (and thus regression) is evaluated through the two-tailed  $t$  test with degrees of freedom corresponding to the number of sample years. The analysis period varies depending on the dataset used, and thus we specify it in a figure caption or the text wherever necessary.

In section 3, we have removed the SST-forced component from the NAUS rainfall anomalies through the same statistical method as in Sekizawa et al. (2018). In this method, we first derive five leading empirical orthogonal functions (EOFs) and principal components (PCs) of tropical (20°S–20°N) SST anomalies averaged over three months including the two target months for the rainfall anomaly and the preceding month (Fig. S2). For example, when applying to JF-mean rainfall, the corresponding EOFs and PCs are obtained based on DJF-mean SST. We then remove the anomalies of NAUS rainfall regressed onto the five SST PCs to obtain the internal component of the rainfall variability as the residual. In fact, Sekizawa et al. (2018) validated this method through comparison with atmospheric general circulation model simulations with climatological-mean SST. As mentioned later, the large-scale SST

influence on NAUS rainfall in JF is extracted primarily in EOF1, and the corresponding PC1 is highly correlated with Niño-3.4 SST. Therefore, in sections 4 and 5, we remove only the regression anomalies onto Niño-3.4 SST to highlight the internal variability of AUSM.

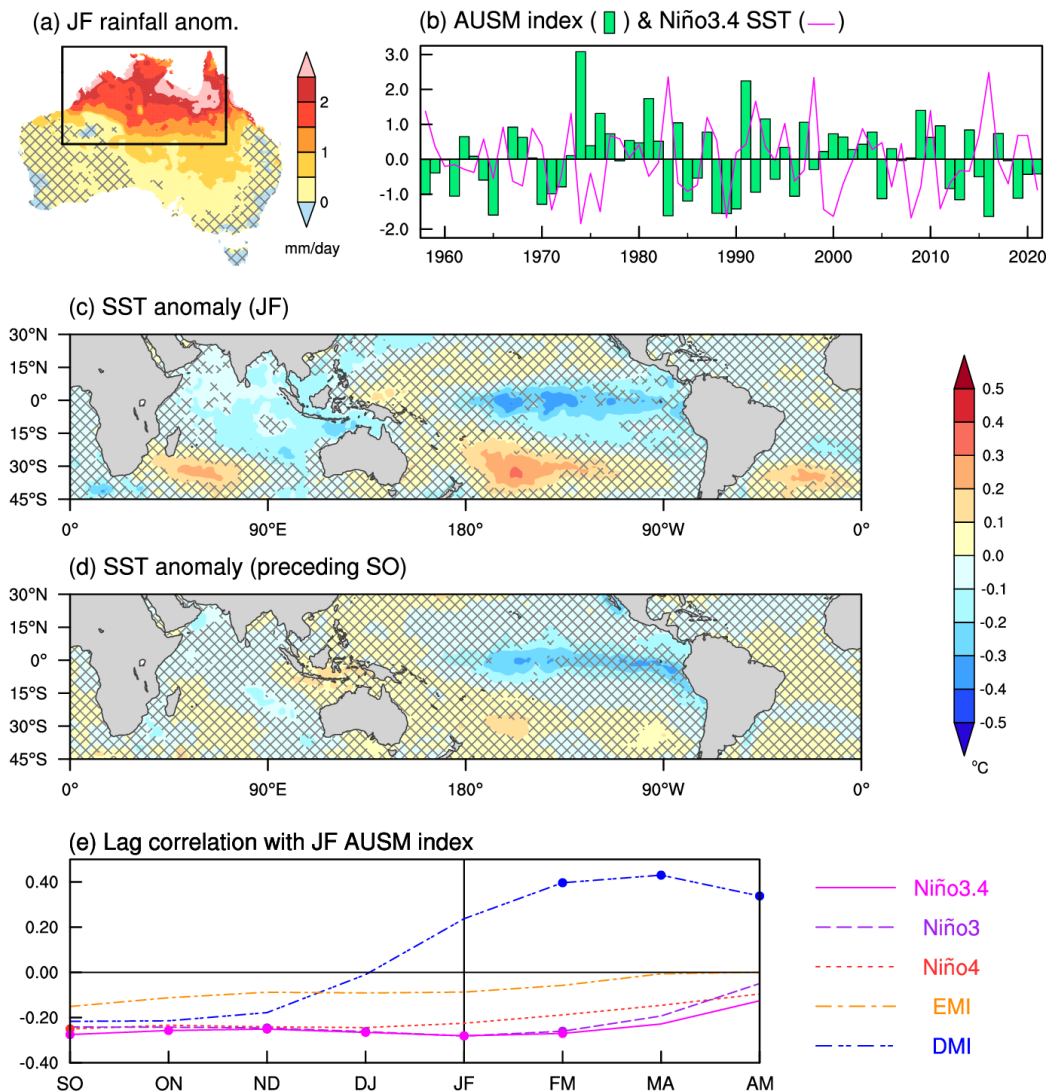


Fig. 1. (a) JF-mean rainfall anomalies based on AWAP (1958–2021) regressed onto the AUSM index (shading). The black rectangle indicates the region for defining our AUSM index. (b) Standardized time series of the AUSM index (green bars) and Niño-3.4 SST (magenta line). (c) JF and (d) preceding September-October mean SST anomalies regressed onto the AUSM index. Areas with significance below the 95% confidence level are hatched in (a), (c) and (d). (e) Lag-correlation coefficients of the AUSM index with various tropical SST indices as indicated. Dots denote significant correlations at the 95% confidence level.

b. MSE budget analysis

MSE is a thermodynamic variable that is approximately conserved in a moist adiabatic process. MSE ( $h$ ) is represented as  $h = c_p T + gz + Lq$ , where  $T$ ,  $z$  and  $q$  denote air temperature, geopotential height and specific humidity, respectively, and constants  $c_p$ ,  $g$ , and  $L$  are the specific heat at constant pressure for air ( $1004.6 \text{ J K}^{-1} \text{ kg}^{-1}$ ), gravitational acceleration ( $9.80665 \text{ m s}^{-2}$ ) and latent heat of vaporization for water ( $2.507 \times 10^6 \text{ J kg}^{-1}$ ), respectively. An equation for the column integrated MSE budget can be expressed as

$$\begin{aligned} \frac{\partial \langle h \rangle}{\partial t} &= - \langle \mathbf{u} \cdot \nabla h \rangle - \langle \omega \frac{\partial h}{\partial p} \rangle + LE + S + \langle R \rangle \\ &= -\nabla \cdot \langle \mathbf{u} h \rangle + Q, \end{aligned} \quad (1)$$

where  $\mathbf{u}$ ,  $\omega$ ,  $E$ ,  $S$  and  $R$  indicate horizontal wind vector, vertical pressure velocity, surface evaporation, surface sensible heat flux and radiative heating rate, respectively (Yanai et al. 1973). Angle brackets denote column integration from the surface to the 100-hPa level. Combining MSE sources into the atmosphere aside from the MSE flux convergence,  $Q = LE + S + \langle R \rangle$  is referred to as an MSE forcing. The MSE tendency at any time step has been calculated as the MSE difference between the concurrent and next time steps of the data.

The MSE flux convergence consists of horizontal and vertical advection terms assuming the vertical flux to be zero at the top of the column. Since the weak temperature gradient approximation usually holds in the tropical troposphere, a strong horizontal gradient of MSE arises mainly from that of humidity in the lower troposphere. Considering that an atmospheric column with lower-level convergence is wetter than the surroundings as a usual situation in active convection, horizontal advection by the incoming flow acts to dry the column and thereby decrease the column-integrated MSE. Meanwhile, the vertical advection depends on the correspondence between the vertical profiles of MSE and divergence. When the MSE at the level of convergence is larger (smaller) than that at the level of divergence, the column-integrated MSE increases (decreases). The MSE is typically larger in the upper troposphere than near the surface, and the vertical profile of upward motion due to deep convective activity forms a single peak in the mid-troposphere. Therefore, the vertical advection by such deep upward motion discharges MSE out of the column, acting to dry the troposphere and decay the convective activity. However, in a situation where the near-surface air is so wet that the MSE difference between the upper and lower troposphere is small, the vertical advection cannot efficiently discharge MSE from the air column, which is suitable for sustaining active convection (Neelin and Held 1987).

Although precipitation does not appear explicitly in Eq. (1), it can be diagnosed through the MSE and moisture budgets. Combining the column-integrated MSE and moisture budget equations and assuming a steady state, we obtain

$$L(P - E) = \frac{Q}{\Gamma}, \quad \text{where} \quad \Gamma \equiv \frac{\nabla \cdot \langle \mathbf{u} h \rangle}{-L \nabla \cdot \langle \mathbf{u} q \rangle}. \quad (2)$$

When precipitation is much larger than evaporation, as typically is the case in a region of active convection,  $P - E \approx P$ . Thus, precipitation can be given by the local MSE forcing  $Q$  divided by normalized gross moist stability (GMS)  $\Gamma$ . The normalized GMS represents the efficiency for the circulation to discharge MSE out of the column by convection of unit intensity (Neelin and Held 1987; Raymond et al. 2009; Inoue and Back 2015), and it can be decomposed into the horizontal and vertical components as

$$\begin{aligned}\Gamma &= \Gamma_h + \Gamma_v \\ &= \frac{\langle \mathbf{u} \cdot \nabla h \rangle}{-L\nabla \cdot \langle \mathbf{u}q \rangle} + \frac{\langle \omega \frac{\partial h}{\partial p} \rangle}{-L\nabla \cdot \langle \mathbf{u}q \rangle}.\end{aligned}\quad (3)$$

The vertical GMS  $\Gamma_v$  indicates the efficiency for the divergence and convergence to discharge MSE through vertical advection, which is related to the vertical profile of MSE, i.e., the vertical stability (corresponding to the original concept of GMS by Neelin and Held 1987). Likewise, the horizontal GMS  $\Gamma_h$  represents the efficiency of discharging MSE due to horizontal advection under the horizontal MSE gradient between the region of interest and its surroundings.

In this study, we have performed the MSE budget analysis for JF-mean MSE anomalies regressed onto the AUSM index based on 6-hourly data from JRA-55 (1958–2021) and daily data from ERA5 (1980–2021). We have confirmed that the JRA-55 results do not change qualitatively if the analysis is limited to the period after 1979 (figure not shown).

### c. OGCM output and mixed-layer heat budget analysis

In our attempt to perform a mixed-layer heat budget analysis to evaluate the effect of the subsurface anomalies on SST anomalies, ocean data with sufficiently high spatiotemporal resolution is required to obtain quantitatively reliable results. For this purpose, we have analyzed the output from a hindcast simulation by an eddy-resolving OGCM for the Earth Simulator (OFES) for 1980–2014 (Sasaki et al. 2008). The model has a horizontal resolution of  $0.1^\circ \times 0.1^\circ$  and 54 vertical levels with 5 to 10-m thickness in upper 200 m, being forced by daily mean momentum, heat and salinity fluxes taken from the National Centers for Environmental Prediction (NCEP) and the National Center for Atmospheric Research (NCAR) atmospheric reanalysis (Kalnay et al. 1996). In the OFES output, fields of temperature, salinity, three-dimensional velocity, surface fluxes are available every 3 days, and therefore it is suited for the following mixed-layer heat budget analysis. Note that the surface salinity field is relaxed to monthly climatology in this OFES simulation.

Following a formulation for the ocean mixed-layer heat budget proposed by Kim et al. (2006), a time tendency of the mixed-layer temperature  $T_m$ , i.e., vertically averaged temperature within the mixed layer, can be expressed as

$$\frac{\partial T_m}{\partial t} = \frac{Q_{net} - q_{SW}}{\rho_w c_w h_m} - [\mathbf{u} \cdot \nabla T]_{ML} - [\mathbf{u} \cdot \nabla T]_{IND} - \left[ w \frac{\partial T}{\partial z} \right] - \frac{\partial h_m}{\partial t} \frac{\Delta T}{h_m}, \quad (4)$$

where square brackets denote vertical averaging down to the mixed-layer bottom. We have defined the mixed-layer depth  $h_m$  at which temperature is lower than SST by  $0.8^\circ\text{C}$ , following Du et al. (2005). Overall results remain qualitatively unchanged if we use the threshold of  $0.5^\circ\text{C}$  instead of  $0.8^\circ\text{C}$  for the definition. The first term on the rhs in Eq. (4) represents heating by the net surface heat fluxes  $Q_{net}$ , where water density  $\rho_w$  ( $=1027 \text{ kg m}^{-3}$ ) and specific heat for water  $c_w$  ( $=4187 \text{ J K}^{-1} \text{ kg}^{-1}$ ) are assumed to be constant. In addition,  $q_{SW}$  indicates shortwave radiation penetrating into subsurface layers, which is estimated through the same parameterization as used in OFES:

$$q_{SW} = Q_{SW} \left\{ R e^{-\frac{h_m}{\xi_1}} + (1 - R) e^{-\frac{h_m}{\xi_2}} \right\},$$

where  $Q_{SW}$  is the net downward surface shortwave radiation, and the parameters  $R$ ,  $\xi_1$  and  $\xi_2$  are set to 0.58, 0.35 m and 23 m, respectively (Paulson and Simpson 1977). The second term of rhs in Eq. (4) represents the temperature advection due to the horizontal flow within the mixed layer, where  $\mathbf{u}$  and  $T$  are horizontal velocity and temperature, respectively. The third through fifth terms represent the entrainment as combined. The third term indicates the horizontal induction, which is the temperature advection due to the horizontal flow crossing the inclined mixed layer bottom and usually small in the maritime domain of our interest. The fourth term denotes the vertical temperature advection, including the effect of shoaling (deepening) isothermal surfaces due to the upwelling (downwelling). Here, the square bracket signifies vertical averaging within the mixed layer. The fifth term is related to the mixed-layer deepening and the associated entrainment of cooler water from below.  $\Delta T$  is locally derived as the difference of vertically averaged temperature between the water remaining in the mixed layer at both the present and next time steps and another water to be entrained or detrained at the next time step (with the 3-day data interval; see Fig. S3). As in the MSE budget analysis, we have evaluated the mixed-layer heat budget for JF-mean anomalies regressed onto the AUSM index.

#### *d. Linear baroclinic model (LBM)*

To examine the local wind response to anomalous diabatic heating over NAUS, we have conducted numerical experiments with an LBM developed by Watanabe and Kimoto (2000). This primitive equation model is linearized about a prescribed three-dimensional basic state to simulate the dry dynamical response to imposed diabatic heating. The following description of the model experiments parallels that of Sekizawa et al. (2021). The model has horizontal and vertical resolutions of T42 and 20 levels in  $\sigma$  coordinates, respectively. In the model we apply biharmonic diffusion with  $e$ -folding time of 1 hour for the largest wavenumber and vertical diffusion with  $e$ -folding time of 1000 days. We also apply linear damping with  $e$ -folding time of 0.5 days in  $\sigma \geq 0.945$  and  $\sigma \leq 0.025$ , 5 days at  $\sigma = 0.900$ , 15 days at  $\sigma = 0.830$  and 30 days in  $0.035 \leq \sigma \leq 0.745$ . We prescribe the JF-mean climatological-mean field as a basic state of the LBM and forced it by the JF-mean anomalies of diabatic heating rate over NAUS (30°–5°S, 105°–160°E) regressed onto the AUSM index, both of which have been derived from JRA-55 (1958–2021). JRA-55 provides three-dimensional diabatic heating fields separately as large-scale and convective condensation, radiative heating and vertical diffusion. We sum them up to use it as forcing. Here, we regard the average of the response from the 31st to 45th days of the integration as the steady response.

### **3. Properties of interannual variability of NAUS rainfall**

#### *a. Relation to the tropical SST variabilities*

Consistent with the previous studies, the AUSM variability has relatively weak linkage to the tropical SST anomalies. Figures 1c and 1d represent JF and September–October (SO)-mean SST anomalies, respectively, regressed onto the JF-mean AUSM index. Typical signatures of

La Niña and Indian Ocean basin-wide cooling develop, but their amplitude and statistical significance are moderate. Indeed, the correlation coefficient between the JF-mean AUSM index and the Niño-3.4 index is  $-0.28$ , which is marginally significant at the 95% confidence level but explains only  $\sim 8\%$  of the variance. At the same time, a cool SST anomaly is conspicuous locally around NAUS in JF, under the enhanced evaporation and less insolation as responses to the stronger AUSM (section 5), indicating the dominance of atmospheric forcing onto the ocean. We can see only weak SST anomalies associated with IOD in austral spring, which is known to exert a significant impact on Australian rainfall (Ashok et al. 2003; Risbey et al. 2009; Cai et al. 2011).

Figure 1e shows lag-correlation coefficients of several tropical SST indices with the JF-mean AUSM index. Consistent with the spatial pattern of SST anomalies as illustrated in Fig. 1c and 1d, the correlations are generally weak despite marginally significant correlations with some of the Pacific SST indices in austral summer and preceding spring. We note that the significant positive correlation between the DMI and AUSM index in JF and the following seasons does not mean a positive IOD development. Rather, this positive correlation merely reflects local cool SST anomalies over the SEIO spreading around the eastern pole of IOD as well as the Indian Ocean basin-wide cooling owing to the weak influence from ENSO (Fig. 1c), resulting in an apparent projection onto DMI.

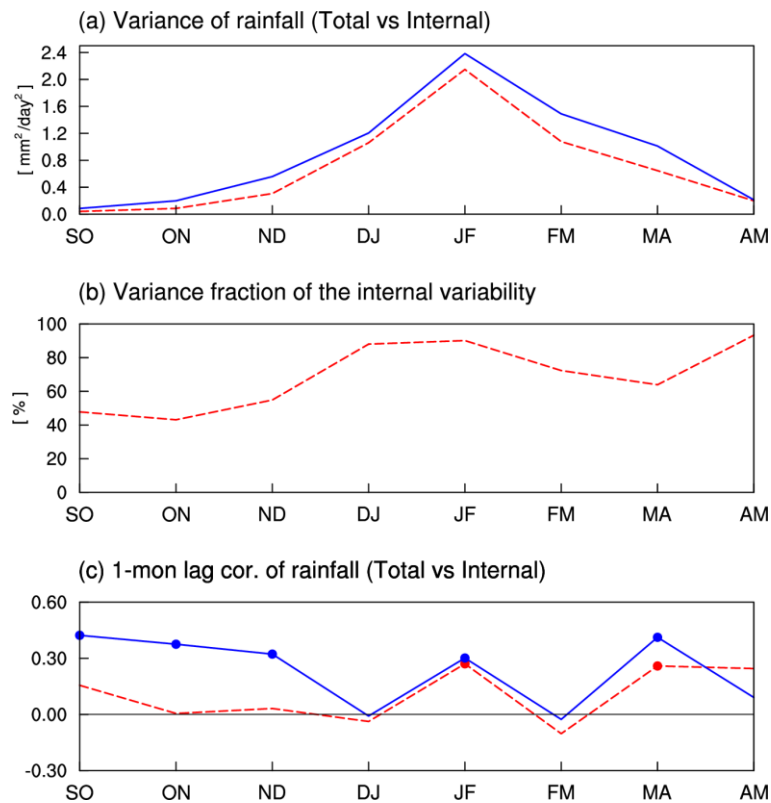


Fig. 2. (a) Interannual variance ( $\text{mm}^2 \text{day}^{-2}$ ) of the total (solid blue line) and internal (dashed red line) component of bimonthly-mean NAUS rainfall averaged over the region denoted in Fig. 1a. (b) Variance fraction (%) of the internal variability to the total variability. (c) One-month lag correlation for the total (solid blue line) and internal (dashed red line) NAUS rainfall anomalies. Dots denote significant correlation at the 95% confidence level. See section 2a for estimation of the internal variability component.

The interannual variances of bimonthly-mean rainfall anomalies over NAUS are shown in Fig. 2a (blue solid line). The variance has a distinct peak in JF, the climatological AUSM season. We have extracted the internal component of NAUS rainfall variability through the statistical method described in section 2a. As in the total variance, the internal variance also peaks in JF (Fig. 2a, red dashed line). The fraction of the internal variance is large in austral summer (exceeding 80%), while it is relatively small in spring and autumn except in April–May (Fig. 2b), consistent with the notion that the influence from tropical SST variability seasonally weakens as the AUSM develops. In JF, the first through fifth PCs of tropical SST have correlation coefficients with the AUSM index of  $-0.28$ ,  $0.09$ ,  $0.08$ ,  $0.01$  and  $0.06$ , respectively. The influence of large-scale SST variability on the JF NAUS rainfall is thus extracted mostly in EOF1, and the other four EOFs do not exert any significant influence. EOF1 represents canonical ENSO (Fig. S2), as the PC1 is almost identical to Niño-3.4 SST (with their correlation at  $+0.98$ ). For simplicity, in sections 4 and 5, we therefore remove only the anomalies correlated to Niño-3.4 SST when extracting the internal variability.

#### *b. Persistence of anomalous rainfall*

If an internal variability is dominant in the variability of JF-mean NAUS rainfall, one may wonder to what extent the internal variability can provide persistence for the anomalous rainfall. To see this, we examine the one-month lag autocorrelation of the NAUS rainfall anomaly (Fig. 2c, blue line). Despite the weaker influence of SST variability in JF (Fig. 2b), rainfall anomalies over NAUS in JF are comparably persistent to that in September–December and March–April. However, the correlation is negligible between December and January, when NAUS usually undergoes the monsoon onset. It is also negligible between February and March, when the monsoon usually retreats. These negligible correlations suggest that processes involved in the rainfall anomalies may differ among the pre-monsoon, monsoon and post-monsoon seasons.

The red dashed line in Fig. 2c shows the one-month lag correlation for the internal component of NAUS rainfall anomalies obtained in a similar manner to that applied to the rainfall variance (Fig. 2a). In austral spring, the correlation for the internal component is substantially weaker than that for the total rainfall variability, consistent with relatively stronger influence from the SST variability (Fig. 2b). In JF, however, the correlation of the internal anomalies is almost the same as that of the total and still statistically significant. These results suggest that the internal variability in the AUSM system can provide a certain level of persistence to the NAUS rainfall anomalies without strong influence from SST variability.

## **4. Mechanisms for the persistent moisture supply**

#### *a. Moisture transport and oceanic evaporation*

Precipitation and 10-m wind anomalies regressed onto the AUSM index (Fig. 3a) feature local intensification of the AUSM system: enhanced convective activity over NAUS and intensified cyclonic circulation. The surface cyclonic anomaly arises as a Rossby-wave response to the enhanced precipitation confined to NAUS (Figs. 3a and 1a; Matsuno 1966; Gill 1980), which is well reproduced in the LBM experiment forced by anomalous diabatic heating regressed onto the AUSM index over NAUS (Fig. 4). In contrast, over the subtropical southern

Indian Ocean ( $\sim 90^\circ\text{E}$ ), convective activity is suppressed in association with the anomalous equatorward winds.

To investigate maintenance mechanisms for the distinct AUSM variability, we first examine the anomalous surface evaporation over the SEIO and moisture transport into NAUS. Associated with the enhanced AUSM activity, anomalous column-integrated water vapor (CWV) flux converges into NAUS from the tropical SEIO (Fig. 3b). The anomalous water vapor flux is cyclonic, following the anomalous surface winds (Fig. 3a). These anomalies suggest that the intensified low-level westerlies bring a greater amount of moisture into the enhanced convection over NAUS from the climatologically warm tropical Indian Ocean.

In association with the intensified moisture transport from the Indian Ocean into NAUS, enhanced evaporation is evident over the tropical SEIO just upstream of the intensified convection over NAUS (Fig. 3b). Through a linearized bulk formula for anomalous surface latent heat flux (LHF), Sekizawa et al. (2018) showed that the enhanced evaporation is primarily induced by the intensified surface wind speed. We have confirmed that the same analysis but for the LHF anomalies regressed onto the AUSM index of the present study yields similar results (see Fig. S4). The associated surface cooling (Fig. 2c) acts to suppress evaporation, but this is well overcome by the contribution from the strengthened surface winds. Figure 3b also depicts significant enhanced evaporation over the central inland region of Australia. We will discuss the role of land-surface evaporation in section 4c.

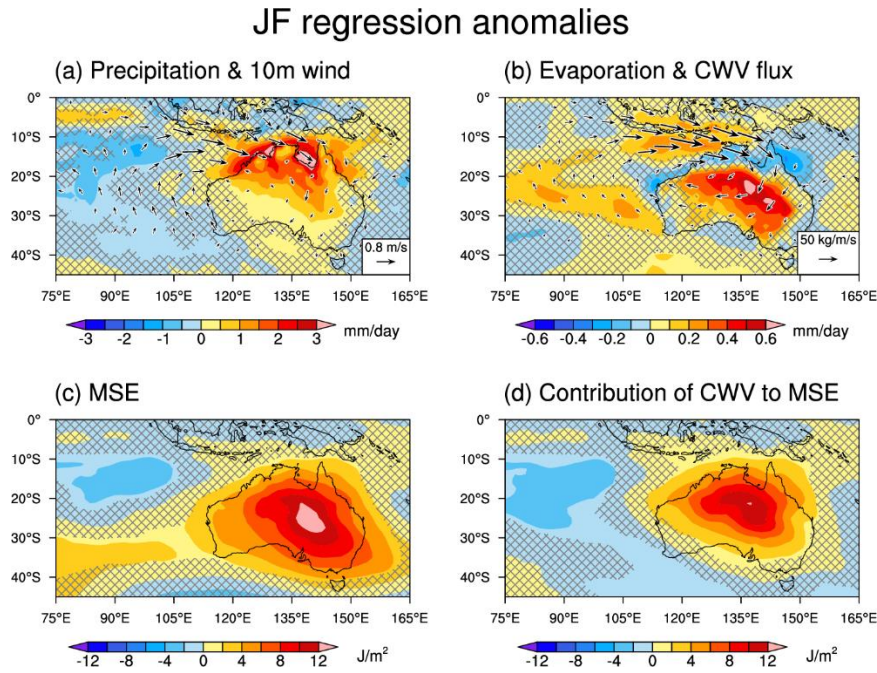


Fig. 3. JF-mean anomalies of (a) precipitation, (b) evaporation, (c) column-integrated MSE and (d) the contribution of CWV to MSE (CWV multiplied by  $L$ ), all regressed onto the AUSM index (shading), based on JRA-55 (1958–2021). Areas with significance below the 95% confidence level are hatched. Vectors in (a) and (b) indicate 10-m wind and CWV flux anomalies, respectively, whose scaling is given at the lower-right corner of each panel. Vectors are plotted only where either the zonal or meridional component is significant at the 95% confidence level.

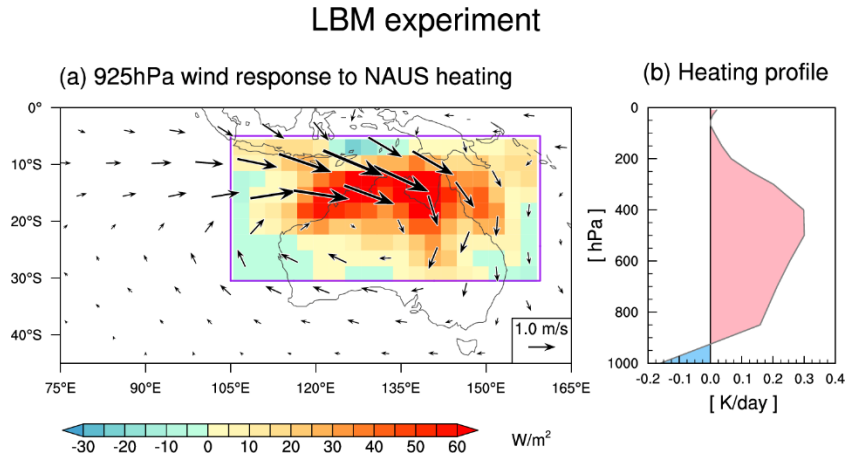


Fig. 4. (a) Steady response of 925-hPa wind (vectors) in the LBM experiment forced by regression anomalies onto the AUSM index of JF-mean three-dimensional diabatic heating, whose column-integrated values are denoted with shading. (b) Vertical profile of the prescribed diabatic heating averaged over the domain marked as the purple box in (a).

### *b. JF-mean MSE budget*

Associated with the strong AUSM, JF-mean MSE significantly increases over the Australian Continent (Fig. 3c). The MSE anomaly is mostly explained by the increased CWV north of 30°S (Fig. 3d), consistent with the assumption of weak temperature gradient in the Tropics. Consistent with the observational fact that tropical precipitation follows an exponential function of the local CWV (Bretherton et al. 2004; Holloway and Neelin 2009), precipitation significantly increases over the region of increased CWV (Figs. 3a and 3d). Indeed, JF-mean rainfall and CWV averaged over NAUS are linearly correlated to each other (Fig. 5a), while they have a clear exponential relationship on daily timescales (Fig. 5b). Persistent rainfall anomalies during JF can be strongly linked with the maintenance of CWV anomalies. To elucidate how the anomalous CWV is maintained over NAUS, we have performed the MSE budget analysis for JF-mean anomalies regressed onto the AUSM index. The column-integrated MSE variability under the weak temperature gradient is mostly characterized by CWV variability, and the MSE budget does not explicitly include the dominant cancellation between the vertical advection of moisture and precipitation in the moisture budget equation. Thus, the MSE budget analysis is useful to diagnose the interaction between convective activity (moisture field) and large-scale circulation in the Tropics (e.g., Andersen and Kuang 2012; Sobel et al. 2014; Ma et al. 2019).

As depicted in Fig. 6a, the JF-mean tendency of MSE anomalies is almost zero everywhere, implying that the anomalous budget is almost balanced as the JF-mean. To see how this balance is achieved, we first look at the MSE flux convergence and forcing anomalies. As shown in Fig. 6c, the anomalous MSE forcing is concentrated in the tropical SEIO, where the intensified monsoonal westerlies and resultant enhanced evaporation are evident (Figs. 3a and 3b). This anomalous MSE forcing is balanced with the anomalous MSE flux divergence (Fig. 6b). By contrast, both anomalous MSE flux divergence and forcing are much weaker over NAUS.

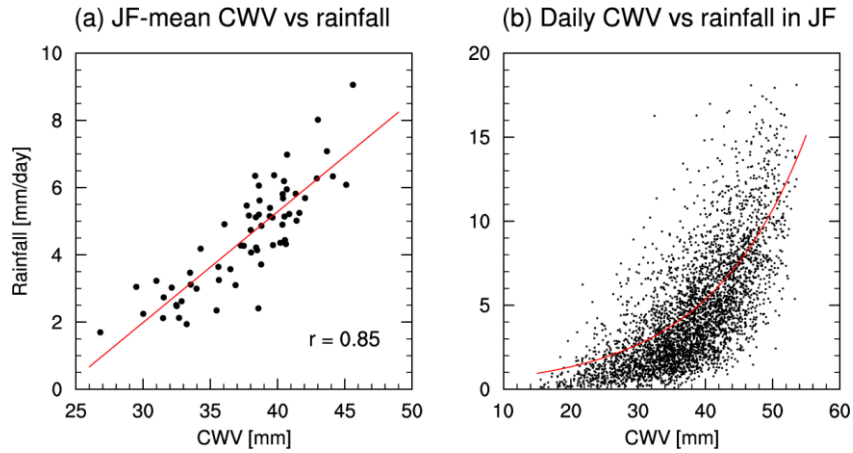


Fig. 5. (a) Scatter plot for JF-mean CWV (JRA-55, 1958–2021) and rainfall (AWAP, 1958–2021) over the NAUS inland domain indicated in Fig. 1a. (b) Same as in (a), but for daily CWV and rainfall in JF. Redlines in (a) and (b) denote linear and exponential fittings, respectively, of CWV-rainfall relationship.

Figures 6d and 6e show decompositions of the anomalous MSE flux divergence and forcing terms, respectively, spatially averaged over the oceanic domain in SEIO and the continental domain in NAUS (denoted in Fig. 6a). The forcing anomaly in SEIO is primarily due to the anomalous LHF and additionally the anomalous longwave heating (Fig. 6e, blue bars). The latter may be caused by reduced outgoing longwave radiation due to the enhanced deep convection, indicating the cloud-radiative feedback. The offsetting MSE tendency through the anomalous flux divergence in this domain is mostly accounted for by the anomalous horizontal advection (Fig. 6d, blue bars). This indicates that a major fraction of the anomalous MSE supply is not consumed by local enhancement of convective activity but balanced by the exportation through the anomalous horizontal advection out of the domain.

Over the continental domain in NAUS, the net-zero anomalous MSE forcing is achieved through the counteracting contributions between enhanced LHF and suppressed sensible heat flux from the wetter and cooler land surface (Fig. 6e, red bars). At the same time, the positive contribution from the horizontal MSE advection is balanced by the negative contribution from the vertical advection (Fig. 6d, red bars). This indicates that the increased MSE through the anomalous horizontal advection is almost totally consumed by the anomalous vertical advection associated with the enhanced convection. As depicted in Fig. 6a, the land domain is located immediately downstream of the oceanic domain under the monsoon westerlies. Therefore, the MSE budget analysis reveals that the anomalous MSE supply to NAUS due to the enhanced evaporation in the SEIO and the intensified monsoon westerlies is expended by the enhanced convective activity. Together with the intensified AUSM circulation by enhanced convective heating (section 4a), our analysis strongly supports the hypothesis that the wind-evaporation-convection feedback sustains the anomalous convection over NAUS (Sekizawa et al. 2018). We have repeated the same analysis with ERA5 (1980–2021) and obtained qualitatively the same results (Fig. S5). Although this kind of analysis could include non-negligible errors, we consider that they do not qualitatively affect the relative importance of those terms.

### MSE budget for JF anomalies

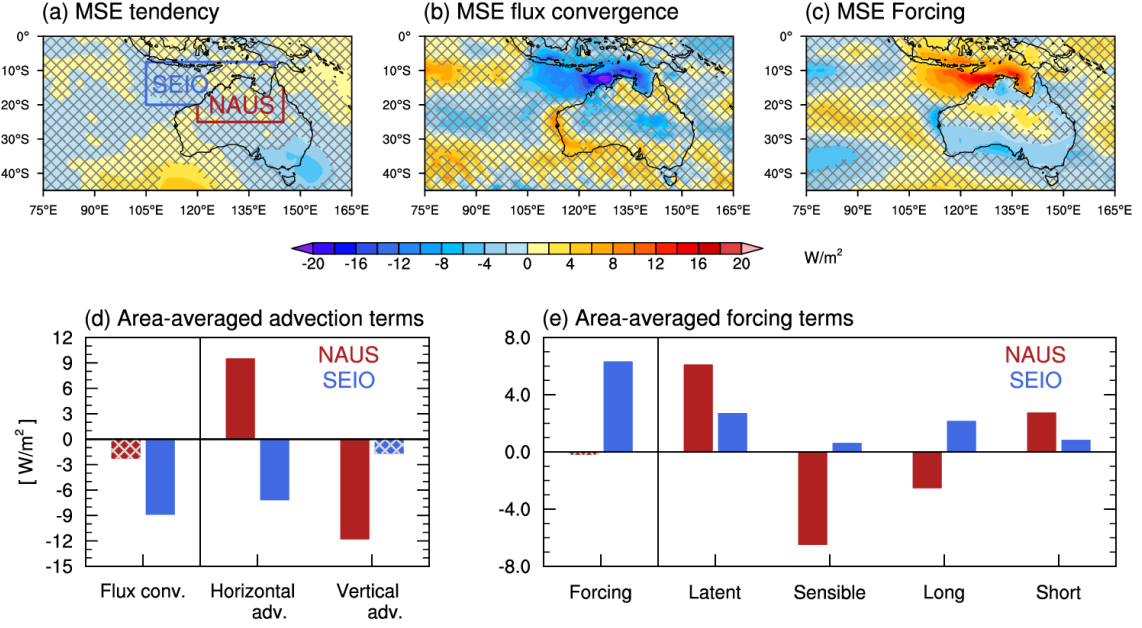


Fig. 6. (a-c) JF-mean anomalies of column-integrated (a) MSE tendency, (b) MSE flux convergence and (c) MSE forcing regressed onto the AUSM index. (d-e) JF-mean anomalies of column-integrated (d, from left to right) net MSE flux convergence, horizontal advection and vertical advection, and (e, from left to right) net MSE forcing, surface LHF, surface sensible heat flux, longwave radiation and shortwave radiation, averaged separately over NAUS (brown bars) and the tropical SEIO (blue bars), regressed onto the AUSM index. All based on JRA-55 (1958–2021). Domains for the spatial averaging are indicated in (a). Hatched areas and bars denote the significance below the 95% confidence level.

Table 1 compares GMS over the NAUS domain in Fig. 6a between the climatology and a typical strong AUSM year. In deriving the climatological GMS, we first calculated the climatologies of area-averaged convergence of the CWV and MSE fluxes separately before taking their ratio. Likewise, we calculated GMS for a typical strong AUSM year by taking their ratio after the regressed anomalies of the CWV and MSE flux convergence had been added to their climatological values. Climatologically, the horizontal GMS is positive, indicating that relatively dry air imported from the outside of the domain acts to weaken the convection. When AUSM is stronger than the climatology, the GMS decreases due to a reduction in its horizontal component. This implies that the anomalously wet inflow from SEIO into NAUS reduces its effect of weakening the convective activity. Meanwhile, the climatological vertical GMS is weakly negative, indicating that convection acts to increase MSE through a slightly unstable vertical profile of MSE. The vertical component becomes closer to zero when the AUSM is strong, implying the relatively stable MSE profile. In terms of GMS [Eqs. (2) and (3)], the fractional change in precipitation can be expressed as

$$\frac{P'}{\bar{P}} = \frac{Q'}{\bar{Q}} - \frac{\Gamma'_h}{\bar{\Gamma}} - \frac{\Gamma'_v}{\bar{\Gamma}}, \quad (5)$$

where an overbar and prime denote JF-mean climatology and an anomaly, respectively. We evaluate the contributions from the individual terms in Eq. (5) to the precipitation change over NAUS under the strong AUSM (Table 1). Consistent with the GMS change, the anomalous precipitation over NAUS is largely accounted for by the reduction in the horizontal GMS. This result reveals that the increased moisture transport from the Indian Ocean is more important for the enhanced NAUS rainfall, rather than local changes in the surface flux or stability.

	$P$ [mm day <sup>-1</sup> ]	$Q$ [W m <sup>-2</sup> ]	$\Gamma$	$\Gamma_h$	$\Gamma_v$
Climatology	5.19	46.5	1.55	1.86	-0.31
Strong AUSM	6.50	46.3	0.97	1.01	-0.03
Fractional change of $P$	+25.3 %	-0.4 %	+37.3 %	+55.1 %	-17.8 %

Table 1. Precipitation ( $P$ ), MSE forcing ( $Q$ ) and GMS ( $\Gamma = \Gamma_h + \Gamma_v$ ) over NAUS in climatology and a typical strong AUSM year based on the regressed anomalies onto the AUSM index (see the text for the details), and corresponding fractional change of precipitation assessed by Eq. (5).

### *c. Soil moisture and land-surface evaporation*

In the previous subsections, we have discussed the anomalous moisture supply from the tropical SEIO associated with the enhanced oceanic evaporation. As shown in Fig. 3, anomalies of rainfall, land-surface evaporation and CWV are not confined to NAUS but extend into the central and eastern inland regions. Our MSE budget analysis has revealed that the net contribution of the anomalous surface heat fluxes is not important over NAUS, where the latent and sensible heat flux anomalies tend to offset each other. Still, the enhanced land-surface evaporation may play a certain role in maintaining the rainfall anomalies especially in the inland regions, as pointed out by previous studies (e.g., Sharmila and Hendon 2020). Thus, we briefly examine the land-surface evaporation and soil moisture anomalies.

Figure 7b illustrates regression anomalies onto the AUSM index of land-surface evapotranspiration at the beginning of February based on AWRA-L. The spatial pattern of land-surface evapotranspiration anomalies well corresponds to that of simultaneous soil moisture anomalies except in the Top End and Cape York Peninsula (Figs. 7b and 7d). By contrast, there are no organized significant anomalies of the variables at the beginning of January (Figs. 7a and 7c). We examine time evolution of the 15-day running-mean anomalous CWV budget over the continental inland domain denoted in Fig. 7b (27.5°–17.5°S, 130°–145°E). The balance between the CWV flux convergence and precipitation anomalies is obvious throughout JF (Fig. 8a, blue and green lines), and therefore the net CWV tendency is much smaller than those offsetting contributions from these two terms (Fig. 8a, black line). In addition, anomalous evaporation makes a secondary positive contribution (Fig. 8a, red line) from mid-January to mid-February with the amplitude of ~50% of the anomalous CWV flux convergence, and its fractional contribution becomes even larger near the end of the AUSM season as the moisture inflow rapidly decreases. Since the land-surface moistening lags the precipitation anomaly (Fig. 8a, shading), the evaporation tends to increase from mid-January two or three weeks after the AUSM onset.

Figures 8b and 8c depict scatter plots between January-mean and February-mean rainfall, and between February 1st soil moisture and February-mean rainfall, respectively, all of which are averaged over the inland domain as indicated in Fig. 7b. Both the January rainfall and February 1st soil moisture are positively correlated with February rainfall. The significant correlation between February 1st soil moisture and February-mean rainfall does not necessarily imply that the anomalous soil moisture provides the persistence of anomalous rainfall from January through February. Rather, the February 1st soil moisture may only be influenced by January rainfall. Nevertheless, we note that February-mean rainfall has stronger correlation

with February 1st soil moisture than with January-mean rainfall, which is significant at the 90% (but not 95%) confidence level based on the paired  $t$  test. These results suggest that the amount of NAUS soil moisture at the beginning of February may possibly influence anomalous February-mean rainfall positively. Since the February 1st soil moisture is largely determined by accumulated rainfall until the end of January, positive feedback, if exists, between rainfall and soil moisture could enhance the persistency of NAUS rainfall anomalies through anomalous land-surface evaporation. More detailed investigation is needed to demonstrate that this memory effect of soil moisture is actually operative.

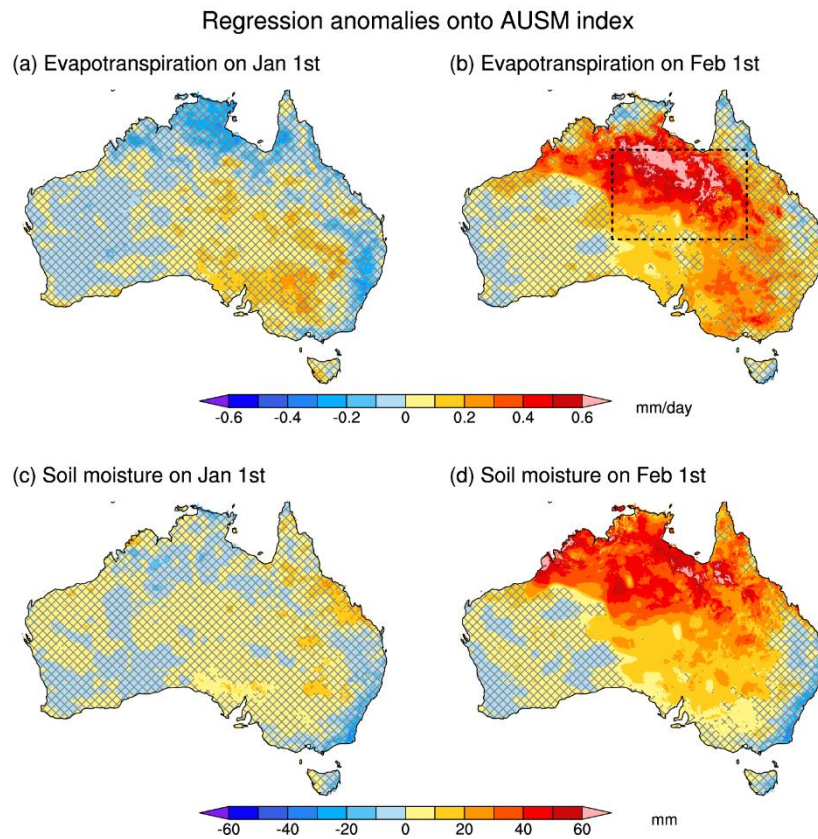


Fig. 7. Regression anomalies onto the AUSM index of (a, b) evapotranspiration and (c, d) soil moisture anomalies on (a, c) January 1st and (b, d) February 1st, based on AWRA-L (1958–2019). Areas with the significance below the 95% confidence level are hatched. Dashed rectangle in (b) indicates the domain for averaging the anomalies in Fig. 8.

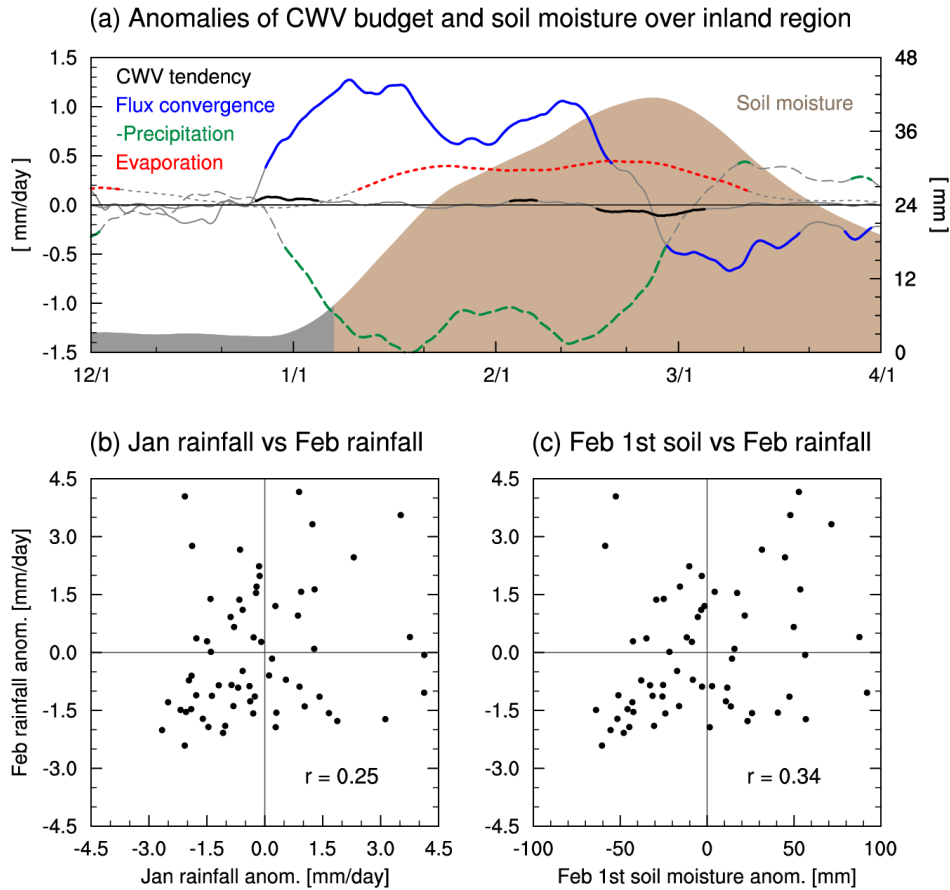


Fig. 8. (a) Regression anomalies (left axis,  $\text{mm day}^{-1}$ ) onto the AUSM index of 15-day running-mean (black line) CWV tendency, (blue) CWV flux convergence, (green) sign-reversed precipitation and (red) evaporation, averaged over the inland domain indicated in Fig. 7b, based on JRA-55 (1958–2021). Brown shading denotes corresponding anomalies of soil moisture (right axis), based on AWRA-L (1958–2019). Gray lines and shading indicate the significance below the 95% confidence level. (b) Scatter plot for January-mean and February-mean rainfall anomalies based on AWAP (1958–2019), averaged over the inland domain (Fig. 7b). (c) Same as in (b), but for February 1st soil moisture and February-mean rainfall anomalies based on AWRA-L and AWAP, respectively (1958–2019).

## 5. Role of air-sea interaction

The influence of the AUSM variability extends into subsurface layers of the tropical SEIO. In the spring (pre-monsoon season) climatology under the prevailing trade easterlies, the thermocline shoals along the Indonesian coast through offshore Ekman transport (Fig. 9a). After the climatological AUSM onset, in contrast, the monsoonal westerlies prevail over this region, deepening both the oceanic mixed layer and thermocline associated with onshore Ekman transport (Fig. 9b). As depicted in Fig. 9c, the anomalously strong AUSM emphasizes these climatological features. The stronger surface westerlies act to cool and thicken the ocean mixed layer through augmented evaporation and mixing, but at the same time they lead to thermocline deepening through intensified Ekman downwelling. The thermocline deepening is manifested as warm anomalies below the mixed layer. Sekizawa et al. (2018) argued that these subsurface anomalies can suppress the SST cooling with resultant negative feedback onto the anomalous evaporation.

To quantify this damping effect, we have performed a mixed-layer heat budget analysis based on the OFES hindcast experiment. We first examine how realistically the hindcast experiment reproduces the seasonal evolution and AISM response of temperature distribution as in the ocean reanalysis (ORA-S5). In comparison of Figs. 9d–f with Figs. 9a–c, one noticeable difference is that the axis of surface wind stress is displaced poleward in OFES, presumably owing to the coarse resolution of the wind field prescribed to the model. Correspondingly, the mixed-layer responses to the anomalous AISM are shifted poleward slightly (Figs. 9c and 9f). In addition, the climatological mixed layer in OFES tends to be cooler by  $\sim 1^\circ\text{C}$  and thicker by  $\sim 5\text{--}10\text{ m}$  than in the reanalysis (Figs. 9b and 9e). Nevertheless, OFES can acceptably reproduce overall temperature distributions for both the climatology and anomalies.

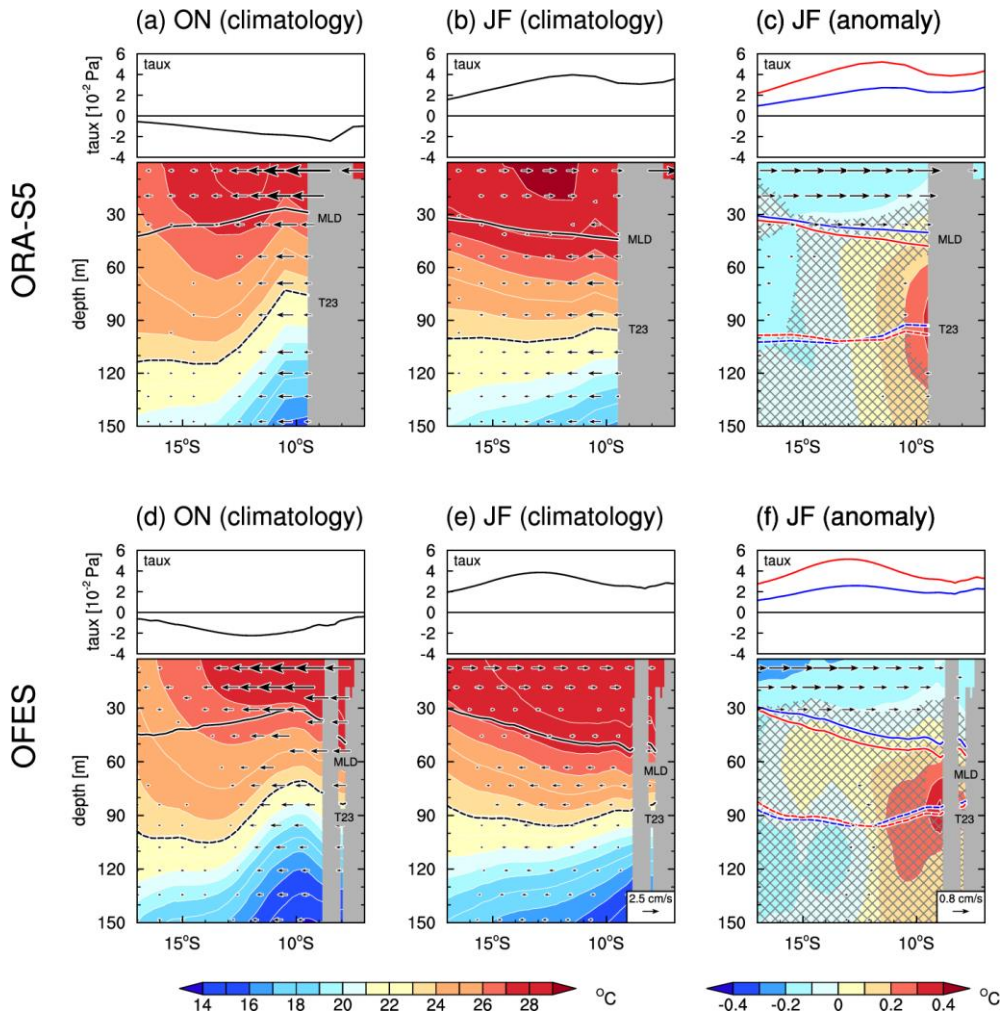


Fig. 9. Meridional sections of longitudinal-mean ( $105^\circ\text{--}125^\circ\text{E}$ ) temperature (shading) and meridional velocity (vectors) for (a, d) ON-climatology, (b, e) JF-climatology and (c, f) JF-mean anomalies regressed onto the AISM index, based on (a–c) ORA-S5 and (d–f) OFES hindcast experiment (1980–2014). Scaling for the vectors is given at the lower-right corner of (e) and (f) for the climatologies and anomalies, respectively. Hatched domains denote the significance of temperature anomalies below the 90% confidence level, and vectors are plotted only where the anomalies are significant at the 90% confidence level. Black lines in (a, b, d, e) indicate the corresponding climatologies of zonal wind stress (upper, solid), the mixed layer bottom (lower, solid) and  $23^\circ\text{C}$  isotherms as a proxy of the thermocline (dashed). Red and blue lines in (c, f) represent their JF-mean anomalies added onto and subtracted from the climatology, respectively.

### Mixed-layer heat budget for JF anomalies

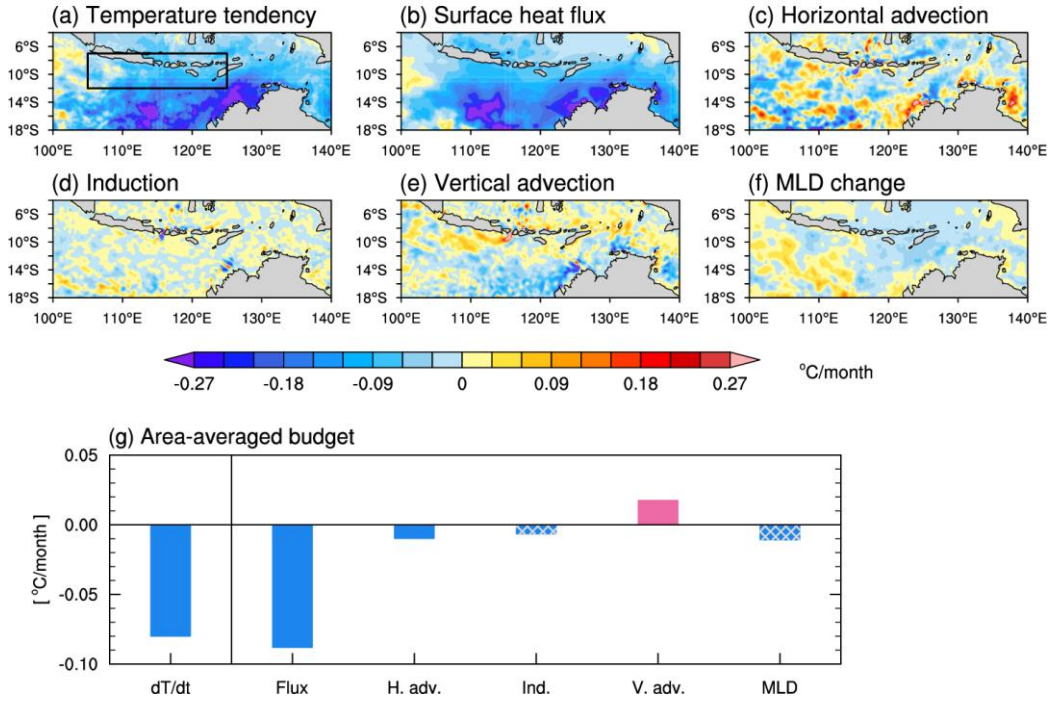


Fig. 10. JF-mean anomalies onto the AUSM index of (a) mixed-layer temperature tendency, and contributions from (b) surface heat flux, (c) horizontal advection in the mixed-layer, (d) induction, (e) vertical advection and (f) temporal evolution of the mixed-layer depth, based on the mixed layer heat budget analysis in Eq. (4) applied to the OFES hindcast experiment. (g) JF-mean anomalies of these terms averaged over the domain indicated with a black box in (a). Hatched bars denote the significance below the 90% confidence level.

Figure 10 exhibits the mixed-layer heat budget for the tropical SEIO based on JF-mean anomalies in the OFES hindcast experiment regressed onto the AUSM index. Associated with the strong AUSM, downward surface heat flux is significantly reduced due to the enhanced evaporation and less insolation, thus acting to cool the mixed layer (Fig. 10b). In fact, the net mixed-layer temperature tendency is mostly attributable to this anomalous surface flux (Fig. 10a). Meanwhile, the anomalous vertical advection acts to warm and cool the mixed layer moderately to the north and south, respectively, of 12°S (Fig. 10e). The latter anomalous cooling tends to be partially offset by the anomalous warming by horizontal advection (Fig. 10c), primarily due to the climatological eastward flow and negative SST anomalies strongest near the NAUS coast (figure not shown). Since the dynamical terms tend to have small-scale features (Figs. 10c–f), we assess the budget based on the spatial averages within the domain [12–7°S, 105–125°E] (black box in Fig. 10a), where the oceanic evaporation is substantially enhanced in a strong AUSM year (Fig. 3b). The anomalous warming due to the vertical advection term cancels out ~20% of the dominant anomalous cooling by the surface heat flux reduction (Fig. 10g). The anomalous mixed-layer deepening also contributes to the mixed-layer cooling, but it is small and statistically insignificant.

The vertical advection term is a product of vertical motion and stratification, and thus its anomaly can be decomposed into the two components as

$$\left[ \left( w \frac{\partial T}{\partial z} \right)' \right] \approx \left[ w' \frac{\partial \bar{T}}{\partial z} \right] + \left[ \bar{w} \frac{\partial T'}{\partial z} \right]. \quad (6)$$

As shown in Figs. 11a and 11b, the anomalous mixed-layer warming that the anomalous vertical advection acts to induce is primarily accounted for by the anomalous vertical motion acting on the mean stratification, whereas the other term makes almost no contribution. This implies that the subsurface warm anomalies under the strong AUSM (Figs. 9c and 9f) do not directly contribute to the anomalous mixed-layer warming. Rather, what is essentially important is the anomalous downward motion induced by the anomalous surface wind stress. Figures 11c and 11d illustrate anomalous vertical motion at the 45.6-m depth and that at the bottom of the Ekman layer (i.e., Ekman pumping velocity)  $w'_E$  estimated from wind stress anomalies as

$$w'_E = \text{curl} \left( \frac{\boldsymbol{\tau}'}{\rho_w f} \right), \quad (7)$$

where  $\boldsymbol{\tau}'$  and  $f$  are anomalous wind stress vector and the Coriolis parameter, respectively. The anomalous anticyclonic (counterclockwise) shear of the wind stress along the equatorward flank of the monsoonal westerlies induces anomalous downward motion along the coast of Indonesia by enhancing the Ekman downwelling (north of  $\sim 12^\circ\text{S}$ , Fig. 11d). Indeed, anomalous vertical velocity at the 45.6-m depth tends to be downward as shown in Fig. 11c. Note that there may be an additional contribution from the reduced coastal upwelling just off the Indonesian coast, which cannot be represented in Eq. (7). Therefore, we can conclude that intensified monsoon westerlies in a strong AUSM year and their anticyclonic shear force anomalous downward motion in the subsurface layer, partially offsetting the anomalous cooling effect of the surface heat fluxes, despite the anomalous deepening of the mixed layer.

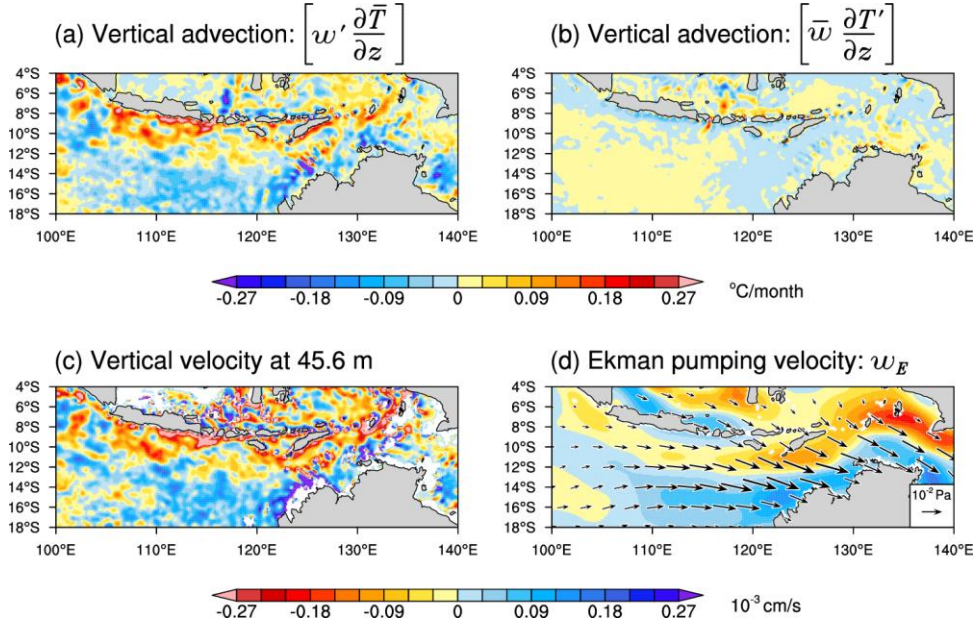


Fig. 11. JF-mean anomalies regressed onto the AUSM index (shading) of the mixed-layer temperature tendencies due to the anomalous vertical advection separately through (a) anomalous vertical velocity acting on the climatological stratification and (b) climatological vertical velocity acting on the anomalous temperature gradient [Eq. (6)], and vertical velocity (c) at the 45.6-m depth and (d) estimated from JF-mean anomalous wind stress (vectors) as the Ekman pumping velocity based on Eq. (7).

## 6. Summary and discussion

The influence of tropical SST variability on NAUS rainfall is known to be weaker in austral summer than in spring. Based on observational data, we have confirmed that internal variability dominates in the interannual variability of mean NAUS rainfall in the AUSM season, whereas the ENSO impact is modest. Despite the relatively weak influence from SST anomalies, the persistence of the rainfall anomaly in January through February is comparable to that between two consecutive months in the pre-monsoon season. This suggests the existence of certain maintenance mechanisms inherent to the AUSM system. In this study, we have investigated the maintenance mechanisms of the AUSM variability and demonstrated its self-sustaining nature under the atmosphere-ocean-land surface interaction, which is illustrated schematically in Fig. 12.

Associated with the stronger AUSM than its climatology, the low-level cyclonic circulation intensifies as a Rossby-wave response to the anomalous diabatic heating over NAUS. The strengthening of the surface monsoon westerlies enhances oceanic evaporation over the tropical SEIO and downstream moisture transport into NAUS. This wind-evaporation feedback is further substantiated through the MSE budget analysis based on reanalysis data. In NAUS with enhanced convective activity, the anomalous vertical advection expends MSE anomalies supplied through the anomalous horizontal advection. This result and associated GMS diagnosis have elucidated that the enhanced convection over NAUS is sustained through the wetter-than-usual low-level inflow from the tropical SEIO rather than local surface heat flux anomalies or a decrease in vertical stability. Meanwhile, in the tropical SEIO, increased MSE exportation due to the horizontal advection is replenished by the locally enhanced MSE forcing, which is accounted for primarily by wind-induced LHF anomalies with an additional contribution of anomalous longwave radiation. Since the monsoon westerlies intensify as a response to the enhanced AUSM convective heating, the present study supports the hypothesis postulated by Sekizawa et al. (2018) that the wind-evaporation-convective feedback sustains the anomalous convection over NAUS as its intrinsic variability.

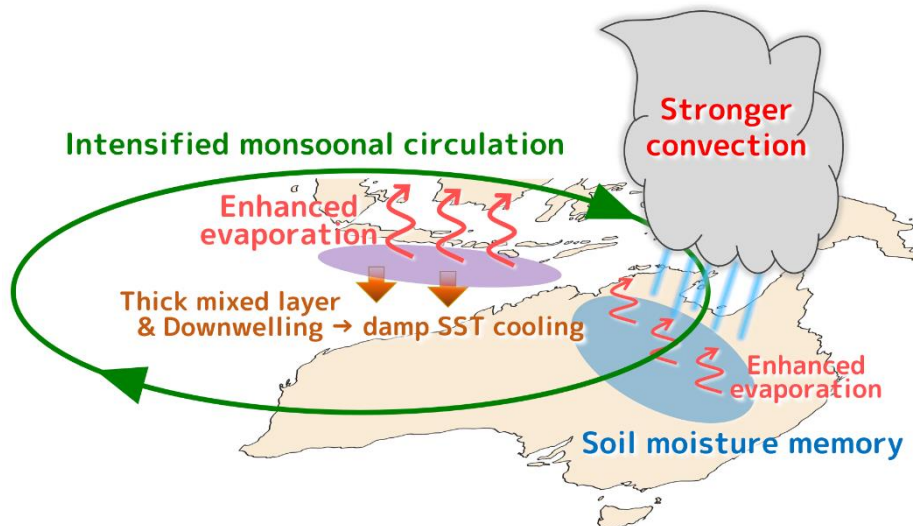


Fig. 12. Schematic of the self-sustaining mechanisms of the AUSM variability, including wind-evaporation-convective feedback, dynamical air-sea interaction and soil moisture memory. This figure features the phase of the stronger AUSM. See the text for details.

These results support the notion that the strengthening of the monsoonal circulation and the resultant evaporation increase are essential for sustaining the anomalous AUSM activity. This feedback mechanism can be considered as a manifestation of the wind-induced surface heat exchange (WISHE; Emanuel 1987; Emanuel et al. 1994), in which the increase in surface heat flux induced by an intensified low-level circulation warms the entire troposphere through the moist convection, feeding back to the atmospheric circulation. Our MSE budget analysis suggests that the maintenance mechanism for the AUSM variability bears some similarity to the moisture mode theory of MJO, where the cloud-radiative feedback and horizontal MSE advection contribute to the maintenance and eastward propagation, respectively, of the MJO convection (e.g., Andersen and Kuang 2012; Zhang et al. 2020; Adames and Maloney 2021). In the AUSM variability, the WISHE mechanism and cloud-radiative feedback act to enhance the convective activity over the tropical SEIO, while the anomalous horizontal advection acts to suppress and enhance it over the SEIO and NAUS to the east, respectively. While the mechanism we have proposed focuses on the AUSM variability that reflects its regional characteristics, a similar mechanism can work in other monsoon systems if it is extended to a more general concept that connects the large-scale circulation, wind-induced oceanic evaporation and continental convection. Ma et al. (2019) focused on the onset of the South Asian Monsoon to reveal the importance of wind-evaporation feedback and cloud-radiative feedback.

For the wind-evaporation feedback mechanism to work effectively, the negative SST anomalies in the tropical SEIO due to the stronger AUSM must be weak enough to prevent evaporation from being reduced. We have investigated ocean current and temperature anomalies in the SEIO and found that the anomalous monsoon westerlies modulate the subsurface vertical motion and associated vertical temperature advection, thereby acting to damp the SST anomalies. This damping effect induced by ocean dynamics has been quantitatively verified through the mixed-layer heat budget analysis. We also note that the seasonal deepening of the mixed layer after the monsoon onset acts to suppress the development of SST anomalies compared to other seasons. In this sense, we consider the AUSM variability to be internal to the coupled AUSM system rather than a pure atmospheric internal variability.

We have also found a significant increase in land-surface evaporation in February associated with the development of soil moisture anomalies in the strong AUSM year, reaching ~50% of the anomalous moisture flux convergence. Our analysis has also shown that, when the soil is wetter (drier) than climatology at the beginning of February, rainfall tends to increase (decrease) in February. This tendency suggests the possible role of soil moisture as a memory for the persistent anomalous rainfall, as pointed out by Sharmila and Hendon (2020). The role of the atmosphere-land surface interaction, as well as the role of the wind-evaporation feedback and ocean dynamics, will be further elucidated in future studies through more detailed analyses of observations, intercomparison of numerical models and sensitivity experiments.

The relationship between AUSM rainfall and ENSO is known to exhibit a clear long-term modulation coherent with the Interdecadal Pacific Oscillation (IPO): stronger correlation in its negative phase and weaker correlation in its positive phase (Power et al. 1999, 2006; Cai et al. 2010; Heidemann et al. 2022). Zhu (2018) attributed this long-term modulation to the Indian Ocean SST change. Therefore, the internal variability we have investigated in this study may also be affected by the long-term modulations of tropical SST, and the influence may be interpreted from the viewpoint of the maintenance mechanisms we have proposed. Future studies may also apply them to interpreting reproducibility and future change of the AUSM variability in climate model simulations.

In this study, we have discussed the maintenance mechanisms of AUSM variability, but its trigger remains to be clarified. As shown in sections 3 and 4, there appears no precursory signal in SST or soil moisture before the onset of the AUSM. This implies that it is difficult to predict the AUSM rainfall with monthly to seasonal leads. Nevertheless, once we identify any signal that could trigger the AUSM variability a few weeks before the onset, it will provide useful predictability on intraseasonal timescales. Especially, it would be worthwhile to investigate the process by which CWV accumulates over the Australian Continent within a relatively short period around the AUSM onset.

### *Acknowledgments*

This work is supported in part by the Japanese Ministry of Education, Culture, Sports, Science and Technology through the Arctic Challenge for Sustainability (ArCS) II Program (JPMXD1420318865), by Japan Society for the Promotion of Science through Grants-in-Aid for Scientific Research JP18H01278, JP19H05702, JP19H05703, JP20H01970, and JP22H01302, by the Japan Science and Technology Agency through COI-NEXT (JPMJPF2013), and by the Ministry of Environment and Environmental Restoration and Conservation Agency of Japan through the Environmental Research and Technology Development Fund (JPMEERF20192004 and JPMEERF20222002). We also acknowledge the assistance of resources from the National Computational Infrastructure supported by the Australian Government. The constructive comments on SS's doctoral dissertation, a part of which is the present paper, by Profs. Y. Masumoto, Y. N. Takayabu, M. Watanabe and H. Miura (University of Tokyo) and discussions with Profs. B. Taguchi (University of Toyama), K. Nishii (Mie University) and Dr. M. Mori (Kyushu University) have been helpful in carrying out this research. The authors also thank Dr. H. Hendon (Australian Bureau of Meteorology), Prof. M. Reeder (Monash University) and their colleagues for useful discussions and allowing to access some local data. Comments from Dr. S. Narsey (Australian Bureau of Meteorology) and two anonymous reviewers are helpful to improve this manuscript.

### *Data Availability Statement*

Australian rainfall datasets are obtained from the Australian Bureau of Meteorology (<http://www.bom.gov.au/climate/data-services/>). The JRA-55 reanalysis datasets are provided by Japan Meteorological Agency ([https://jra.kishou.go.jp/JRA-55/index\\_en.html](https://jra.kishou.go.jp/JRA-55/index_en.html)), HadISST data by Met Office Hadley Centre (<http://www.metoffice.gov.uk/hadobs/hadisst/>), ORA-S5 datasets by ECMWF (<https://www.ecmwf.int/en/research/climate-reanalysis/ocean-reanalysis>). NCAR Command Language (<http://dx.doi.org/10.5065/D6WD3XH5>) version 6.5.0 has been used for the analyses and visualizations.

## REFERENCES

- Adames, Á. F., E. D. Maloney, 2021: Moisture mode theory's contribution to advances in our understanding of the Madden-Julian Oscillation and other tropical disturbances. *Curr. Climate Change Rep.*, **7**, 72–85, <https://doi.org/10.1007/s40641-021-00172-4>.
- Andersen, J. A., and Z. Kuang, 2012: Moist static energy budget of MJO-like disturbances in the atmosphere of a zonally symmetric aquaplanet, *J. Climate*, **25**, 2782–2804, <https://doi.org/10.1175/JCLI-D-11-00168.1>.
- Ashok, K., S. K. Behera, S. A. Rao, H. Weng, and T. Yamagata, 2007: El Niño Modoki and its possible teleconnection. *J. Geophys. Res.*, **112**, C11007, <https://doi.org/10.1029/2006JC003798>.
- \_\_\_\_\_, Z. Guan, and T. Yamagata, 2003: Influence of the Indian Ocean Dipole on the Australian winter rainfall. *Geophys. Res. Lett.*, **30**, 1821, <https://doi.org/10.1029/2003GL017926>.
- Berry, G., M. J. Reeder, and C. Jakob, 2011: Physical mechanisms regulating summertime rainfall over northwestern Australia, *J. Climate*, **24**, 3705–3717, <https://doi.org/10.1175/2011JCLI3943.1>.
- Bowman, D., 2002: The Australian summer monsoon: a biogeographic perspective. *Australian Geographical Studies*, **40**, 261–277. <https://doi.org/10.1111/1467-8470.00179>.
- Bretherton, C. S., M. E. Peters, and L. E. Back, 2004: Relationships between water vapor path and precipitation over the tropical oceans, *J. Climate*, **17**, 1517–1528, [https://doi.org/10.1175/1520-0442\(2004\)017%3C1517:RBWVPA%3E2.0.CO;2](https://doi.org/10.1175/1520-0442(2004)017%3C1517:RBWVPA%3E2.0.CO;2).
- Cai, W., P. van Rensch, T. Cowan, and A. Sullivan, 2010: Asymmetry in ENSO teleconnection with regional rainfall, its multidecadal variability, and impact. *J. Climate*, **23**, 4944–4955, <http://doi.org/10.1175/2010JCLI3501.1>.
- \_\_\_\_\_, \_\_\_\_\_, \_\_\_\_\_, and H. H. Hendon, 2011: Teleconnection pathways of ENSO and the IOD and the mechanisms for impacts on Australian rainfall, *J. Climate*, **24**, 3910–3923, <https://doi.org/10.1175/2011JCLI4129.1>.
- Drosowsky, W., 1996: Variability of the Australian summer monsoon at Darwin: 1957–1992. *J. Climate*, **9**, 85–96, [http://doi.org/10.1175/1520-0442\(1996\)009<0085:VOTASM>2.0.CO;2](http://doi.org/10.1175/1520-0442(1996)009<0085:VOTASM>2.0.CO;2).
- \_\_\_\_\_, and M. Williams, 1991: The Southern Oscillation in the Australian region. Part I: Anomalies at the extremes of the oscillation. *J. Climate*, **4**, 619–638, [http://doi.org/10.1175/1520-0442\(1991\)004<0619:TSOITA>2.0.CO;2](http://doi.org/10.1175/1520-0442(1991)004<0619:TSOITA>2.0.CO;2).
- Du, Y., T. Qu, G. Meyers, Y. Masumoto, and H. Sasaki, 2005: Seasonal heat budget in the mixed layer of the southeastern tropical Indian Ocean in a high-resolution ocean general circulation model. *J. Geophys. Res.*, **110**, C04012, <https://doi.org/10.1029/2004JC002845>.
- Emanuel, K. A., 1987: An air-sea interaction model of intraseasonal oscillations in the tropics. *J. Atmos. Sci.*, **44**, 2324–2340, [https://doi.org/10.1175/1520-0469\(1987\)044<2324:AASIMO>2.0.CO;2](https://doi.org/10.1175/1520-0469(1987)044<2324:AASIMO>2.0.CO;2).
- \_\_\_\_\_, J. D. Neelin, and C. S. Bretherton, 1994: On large-scale circulations in convecting atmospheres. *Quart. J. Roy. Meteor. Soc.*, **120**, 1111–1143, <https://doi.org/10.1002/qj.49712051902>.
- Evans, S., R. Marchand, and T. Ackerman, 2014: Variability of the Australian monsoon and precipitation trends at Darwin. *J. Climate*, **27**, 8487–8500, <http://doi.org/10.1175/JCLI-D-13-00422.1>.
- Frost, A. J., A. Ramchurn, and A. Smith, 2018: The Australian landscape water balance model (AWRAL v6). Technical description of the Australian water resources assessment landscape model version 6, [http://www.bom.gov.au/water/landscape/assets/static/publications/AWRALv6\\_Model\\_Description\\_Report.pdf](http://www.bom.gov.au/water/landscape/assets/static/publications/AWRALv6_Model_Description_Report.pdf).

- Gill, A. E., 1980: Some simple solutions for heat-induced tropical circulation. *Quart. J. Roy. Meteor. Soc.*, **106**, 447–462, <http://doi.org/10.1002/qj.49710644905>.
- Heidemann, H., J. Ribbe, T. Cowan, B. J. Henley, C. Pudmenzky, R. Stone, and D. H. Cobon, 2022: The influence of interannual and decadal Indo-Pacific sea surface temperature variability on Australian monsoon rainfall, *J. Climate*, **35**, 425–444, <https://doi.org/10.1175/JCLI-D-21-0264.1>.
- Hendon, H. H., and B. Liebmann, 1990a: A composite study of onset of the Australian summer monsoon, *J. Atmos. Sci.*, **47**, 2227–2240, [http://doi.org/10.1175/1520-0469\(1990\)047<2227:ACSOOO>2.0.CO;2](http://doi.org/10.1175/1520-0469(1990)047<2227:ACSOOO>2.0.CO;2).
- \_\_\_\_\_, and \_\_\_\_\_, 1990b: The intraseasonal (30–50 day) oscillation of the Australian summer monsoon. *J. Atmos. Sci.*, **47**, 2909–2923, [http://doi.org/10.1175/1520-0469\(1990\)047<2909:TIDOOT>2.0.CO;2](http://doi.org/10.1175/1520-0469(1990)047<2909:TIDOOT>2.0.CO;2).
- \_\_\_\_\_, E.-P. Lim, and G. Liu, 2012: The role of air-sea interaction for prediction of Australian summer monsoon rainfall. *J. Climate*, **25**, 1278–1290, <http://doi.org/10.1175/JCLI-D-11-00125.1>.
- Hersbach, H., and Coauthors, 2020: The ERA5 global reanalysis. *Quart. J. Roy. Meteor. Soc.*, **146**, 1999–2049, <https://doi.org/10.1002/qj.3803>.
- Holland, G. J., 1986: Interannual variability of the Australian summer monsoon at Darwin: 1952–82. *Mon. Wea. Rev.*, **114**, 594–604, [http://doi.org/10.1175/1520-0493\(1986\)114<0594:IVOTAS>2.0.CO;2](http://doi.org/10.1175/1520-0493(1986)114<0594:IVOTAS>2.0.CO;2).
- Holloway, C. E., and J. D. Neelin, 2009: Moisture vertical structure, column water vapor, and tropical deep convection, *J. Atmos. Sci.*, **66**, 1665–1683, <https://doi.org/10.1175/2008JAS2806.1>.
- Howden S. M., S. J. Crimp, C. J. Stokes, 2008: Climate change and Australian livestock systems: impacts, research and policy issues. *Australian J. Experimental Agriculture*, **48**, 780–788, <https://doi.org/10.1071/EA08033>.
- Inoue, K., and L. Back, 2015: Column-integrated moist static energy budget analysis on various time scales during TOGA COARE. *J. Atmos. Sci.*, **72**, 1856–1871, <https://doi.org/10.1175/JAS-D-14-0249.1>.
- Jones, D., W. Wang, and R. Fawcett, 2009: High-quality spatial climate data-sets for Australia. *Australian Meteor. Ocean. J.*, **58**, 233–248, <http://doi.org/10.22499/2.5804.003>.
- Kajikawa, Y., B. Wang, and J. Yang, 2010: A multi-time scale Australian monsoon index. *Int. J. Climatol.*, **30**, 1114–1120, <http://doi.org/10.1002/joc.1955>.
- Kalnay, E., M. Kanamitsu, R. Kistler, W. Collins, D. Deaven, L. Gandin, M. Iredell, S. Saha, G. White, J. Woollen, Y. Zhu, M. Chelliah, W. Ebisuzaki, W. Higgins, J. Janowiak, K.C. Mo, C. Ropelewski, A. Leetmaa, R. Reynolds, and R. Jenne, 1996: The NCEP/NCAR 40-year reanalysis project. *Bull. Amer. Meteor. Soc.*, **77**, 437–471, [https://doi.org/10.1175/1520-0477\(1996\)077<0437:TNYRP>2.0.CO;2](https://doi.org/10.1175/1520-0477(1996)077<0437:TNYRP>2.0.CO;2).
- Kawamura, R., Y. Fukuta, H. Ueda, T. Matsuura, and S. Iizuka, 2002: A mechanism of the onset of the Australian summer monsoon, *J. Geophys. Res.*, **107**, <http://doi.org/10.1029/2001JD001070>.
- Kim, S.-B., I. Fukumori, and T. Lee, 2006: The closure of the ocean mixed layer temperature budget using level-coordinate model fields. *J. Atmos. Ocean. Technol.*, **23**, 840–853, <https://doi.org/10.1175/JTECH1883.1>.
- Kobayashi, S., Y. Ota, Y. Harada, A. Ebata, M. Moriya, H. Onoda, K. Onogi, H. Kamahori, C. Kobayashi, H. Endo, K. Miyaoka, and K. Takahashi, 2015: The JRA-55 Reanalysis: General specifications and basic characteristics. *J. Meteor. Soc. Japan*, **93**, 5–48, <http://doi.org/10.2151/jmsj.2015-001>.

- Larkin, N. K., and D. E. Harrison, 2002: ENSO warm (El Niño) and cold (La Niña) event life cycles: ocean surface anomaly patterns, their symmetries, asymmetries, and implications. *J. Climate*, **15**, 1118–1140, [http://doi.org/10.1175/1520-0442\(2002\)015<1118:EWENOA>2.0.CO;2](http://doi.org/10.1175/1520-0442(2002)015<1118:EWENOA>2.0.CO;2).
- Lo, F., M. C. Wheeler, H. Meinke, and A. Donald, 2007: Probabilistic forecasts of the onset of the north Australian wet season, *Mon. Wea. Rev.*, **135**, 3506–3520, <https://doi.org/10.1175/MWR3473.1>.
- Ma, D., A. H. Sobel, Z. Kuang, M. S. Singh, and J. Nie, 2019: A moist entropy budget view of the South Asian summer monsoon onset. *Geophys. Res. Lett.*, **46**, 4476–4484, <https://doi.org/10.1029/2019GL082089>.
- Martius, O., K. Wehrli, and M. Rohrer, 2021: Local and remote atmospheric responses to soil moisture anomalies in Australia. *J. Climate*, **34**, 9115–9131, <https://doi.org/10.1175/JCLI-D-21-0130.1>.
- Matsuno, T., 1966: Quasi-geostrophic motions in the equatorial area. *J. Meteor. Soc. Japan.*, **44**, 25–43, [https://doi.org/10.2151/jmsj1965.44.1\\_25](https://doi.org/10.2151/jmsj1965.44.1_25).
- Meehl, G. A., 1987: The annual cycle and interannual variability in the tropical Pacific and Indian Ocean regions. *Mon. Wea. Rev.*, **115**, 27–50, [http://doi.org/10.1175/1520-0493\(1987\)115<0027:TACAIV>2.0.CO;2](http://doi.org/10.1175/1520-0493(1987)115<0027:TACAIV>2.0.CO;2).
- Mitchell, T. P., and J. M. Wallace, 1992: The annual cycle in equatorial convection and sea surface temperature. *J. Climate*, **5**, 1140–1156, [http://doi.org/10.1175/1520-0442\(1992\)005<1140:TACIEC>2.0.CO;2](http://doi.org/10.1175/1520-0442(1992)005<1140:TACIEC>2.0.CO;2).
- Mollah, W. S., and I. M. Cook, 1996: Rainfall variability and agriculture in the semi-arid tropics—the Northern Territory, Australia. *Agricultural and Forest Meteorol.*, **79**, 39–60, [https://doi.org/10.1016/0168-1923\(95\)02267-8](https://doi.org/10.1016/0168-1923(95)02267-8).
- Narsey, S., M. J. Reeder, D. Ackerley, and C. Jakob, 2017: A midlatitude influence on Australian monsoon bursts, *J. Climate*, **30**, 5377–5393, <https://doi.org/10.1175/JCLI-D-16-0686.1>.
- Neelin, J. D., and I. M. Held, 1987: Modeling tropical convergence based on the moist static energy budget. *Mon. Wea. Rev.*, **115**, 3–12, [https://doi.org/10.1175/1520-0493\(1987\)115<0003:MTCBOT>2.0.CO;2](https://doi.org/10.1175/1520-0493(1987)115<0003:MTCBOT>2.0.CO;2).
- Paulson, C. A., and J. J. Simpson, 1977: Irradiance measurements in the upper ocean. *J. Phys. Oceanogr.*, **7**, 952–956, [https://doi.org/10.1175/1520-0485\(1977\)007<0952:IMITUO>2.0.CO;2](https://doi.org/10.1175/1520-0485(1977)007<0952:IMITUO>2.0.CO;2).
- Power, S., T. Casey, C. Folland, A. Colman, and V. Mehta, 1999: Inter-decadal modulation of the impact of ENSO on Australia. *Climate Dyn.*, **15**, 319–324, <https://doi.org/10.1007/s003820050284>.
- \_\_\_\_\_, M. Haylock, R. Colman, and X. Wang, 2006: The predictability of interdecadal changes in ENSO activity and ENSO teleconnections. *J. Climate*, **19**, 4755–4771, <https://doi.org/10.1175/JCLI3868.1>.
- Raymond, D. J., S. L. Sessions, A. H. Sobel, and Ž. Fuchs, 2009: The mechanics of Gross Moist Stability. *J. Adv. Model. Earth Syst.*, **1**, 9, <https://doi.org/10.3894/JAMES.2009.1.9>.
- Rayner, N. A., D. E. Parker, E. B. Horton, C. K. Folland, L. V. Alexander, D. P. Rowell, E. C. Kent, and A. Kaplan, 2003: Global analyses of sea surface temperature, sea ice, and night marine air temperature since the late nineteenth century. *J. Geophys. Res.*, **108**, 4407, <http://doi.org/10.1029/2002JD002670>.
- Risbey, J. S., M. J. Pook, P. C. McIntosh, M. C. Wheeler, and H. H. Hendon, 2009: On the remote drivers of rainfall variability in Australia. *Mon. Wea. Rev.*, **137**, 3233–3253, <http://doi.org/10.1175/2009MWR2861.1>.
- Saji, N. H., B. N. Goswami, P. N. Vinayachandran, and T. Yamagata, 1999: A dipole in the tropical Indian Ocean. *Nature*, **401**, 360–363, <http://doi.org/10.1038/43854>.

- Sasaki H., M. Nonaka, Y. Masumoto, Y. Sasai, H. Uehara, and H. Sakuma, 2008: An eddy-resolving hindcast simulation of the quasiglobal ocean from 1950 to 2003 on the Earth Simulator. In: Hamilton K., Ohfuchi W. (eds) High Resolution Numerical Modelling of the Atmosphere and Ocean. Springer, New York, NY. [https://doi.org/10.1007/978-0-387-49791-4\\_10](https://doi.org/10.1007/978-0-387-49791-4_10).
- Sekizawa, S., H. Nakamura, and Y. Kosaka, 2018: Interannual variability of the Australian summer monsoon system internally sustained through wind-evaporation feedback. *Geophys. Res. Lett.*, **45**, 7748–7755, <http://doi.org/10.1029/2018GL078536>.
- \_\_\_\_\_, \_\_\_\_\_, and \_\_\_\_\_, 2021: Remote influence of the interannual variability of the Australian summer monsoon on wintertime climate in East Asia and the western North Pacific, *J. Climate*, **34**, 9551–9570, <https://doi.org/10.1175/JCLI-D-21-0202.1>.
- Sharmila, S., and H. H. Hendon, 2020: Mechanisms of multiyear variations of northern Australia wet-season rainfall. *Sci. Rep.*, **10**, 5086, <http://doi.org/10.1038/s41598-020-61482-5>.
- Sobel, A., S. Wang, and D. Kim, 2014: Moist static energy budget of the MJO during DYNAMO, *J. Atmos. Sci.*, **71**, 4276–4291, <https://doi.org/10.1175/JAS-D-14-0052.1>.
- Suppiah, R., 1992: The Australian summer monsoon: a review. *Prog. Phys. Geogr.: Earth and Environment*, **16**, 283–318, <http://doi.org/10.1177/030913339201600302>.
- Taschetto, A. S., A. S. Gupta, H. H. Hendon, C. C. Ummenhofer, and M. H. England, 2011: The contribution of Indian Ocean sea surface temperature anomalies on Australian summer rainfall during El Niño events. *J. Climate*, **24**, 3734–3747, <https://doi.org/10.1175/2011JCLI3885.1>.
- Watanabe, M., and M. Kimoto, 2000: Atmosphere-ocean thermal coupling in the North Atlantic: A positive feedback. *Quart. J. Roy. Meteor. Soc.*, **126**, 3343–3369, <https://doi.org/10.1002/qj.49712657017>.
- Wheeler, M. C., H. H. Hendon, S. Cleland, H. Meinke, and A. Donald, 2009: Impacts of the Madden–Julian Oscillation on Australian rainfall and circulation. *J. Climate*, **22**, 1482–1498, <http://doi.org/10.1175/2008JCLI2595.1>.
- Wu, R., and B. P. Kirtman, 2007: Roles of the Indian Ocean in the Australian summer monsoon-ENSO relationship. *J. Climate*, **20**, 4768–4788, <https://doi.org/10.1175/JCLI4281.1>.
- Xie, S.-P., and S. G. H. Philander, 1994: A coupled ocean-atmosphere model of relevance to the ITCZ in the eastern Pacific. *Tellus A*, **46**, 340–350, <http://doi.org/10.3402/tellusa.v46i4.15484>.
- Yanai, M., S. Esbensen, and J. Chu, 1973: Determination of bulk properties of tropical cloud clusters from large-scale heat and moisture budgets. *J. Atmos. Sci.*, **30**, 611–627, [https://doi.org/10.1175/1520-0469\(1973\)030<0611:DOBPOT>2.0.CO;2](https://doi.org/10.1175/1520-0469(1973)030<0611:DOBPOT>2.0.CO;2).
- Zhang, C., Á. F. Adames, B. Khouider, B. Wang, and D. Yang, 2020: Four theories of the Madden-Julian Oscillation. *Rev. Geophys.*, **58**, e2019RG000685, <https://doi.org/10.1029/2019RG000685>.
- Zhu, Z., 2018: Breakdown of the relationship between Australian summer rainfall and ENSO caused by tropical Indian Ocean SST warming. *J. Climate*, **31**, 2321–2336. <https://doi.org/10.1175/JCLI-D-17-0132.1>.
- Zuo, H., M. A. Balmaseda, S. Tietsche, K. Mogensen, and M. Mayer, 2019: The ECMWF operational ensemble reanalysis–analysis system for ocean and sea ice: a description of the system and assessment, *Ocean Sci.*, **15**, 779–808, <https://doi.org/10.5194/os-15-779-2019>.

## Supplemental figures

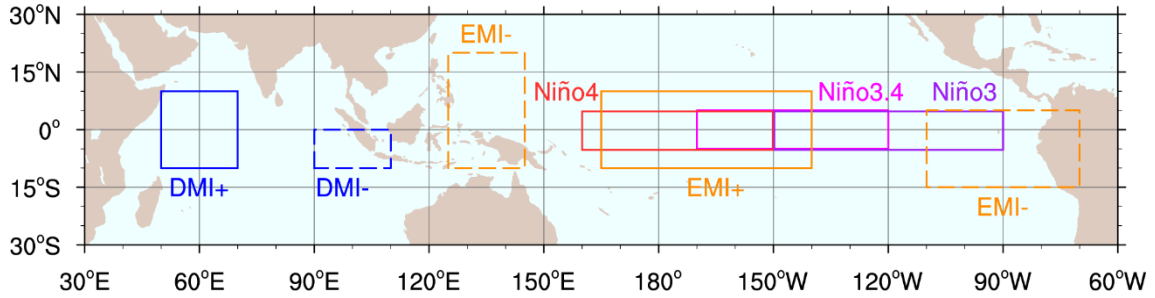


Fig. S1. Domains for the definitions of tropical SST indices. Purple, magenta, red, orange and blue boxes denote the domains for Niño3, Niño3.4, Niño4, EMI and DMI, respectively. SST anomalies in solid and dashed rectangles contribute positively and negatively, respectively, to the corresponding indices. Let  $x(A)$  be SST anomaly averaged over domain  $A$ , these indices are defined as the following:

$$\text{Niño3 index} = x(5^{\circ}\text{S}–5^{\circ}\text{N}, 150^{\circ}–90^{\circ}\text{W})$$

$$\text{Niño3.4 index} = x(5^{\circ}\text{S}–5^{\circ}\text{N}, 170^{\circ}–120^{\circ}\text{W})$$

$$\text{Niño4 index} = x(5^{\circ}\text{S}–5^{\circ}\text{N}, 160^{\circ}\text{E}–150^{\circ}\text{W})$$

$$\text{EMI} = x(10^{\circ}\text{S}–10^{\circ}\text{N}, 165^{\circ}\text{E}–140^{\circ}\text{W}) - 0.5 \times x(10^{\circ}\text{S}–20^{\circ}\text{N}, 125^{\circ}–145^{\circ}\text{E}) \\ - 0.5 \times x(15^{\circ}\text{S}–5^{\circ}\text{N}, 110^{\circ}–70^{\circ}\text{W})$$

$$\text{DMI} = x(10^{\circ}\text{S}–10^{\circ}\text{N}, 50^{\circ}–70^{\circ}\text{E}) - x(10^{\circ}\text{S}–\text{EQ}, 90–110^{\circ}\text{E}).$$

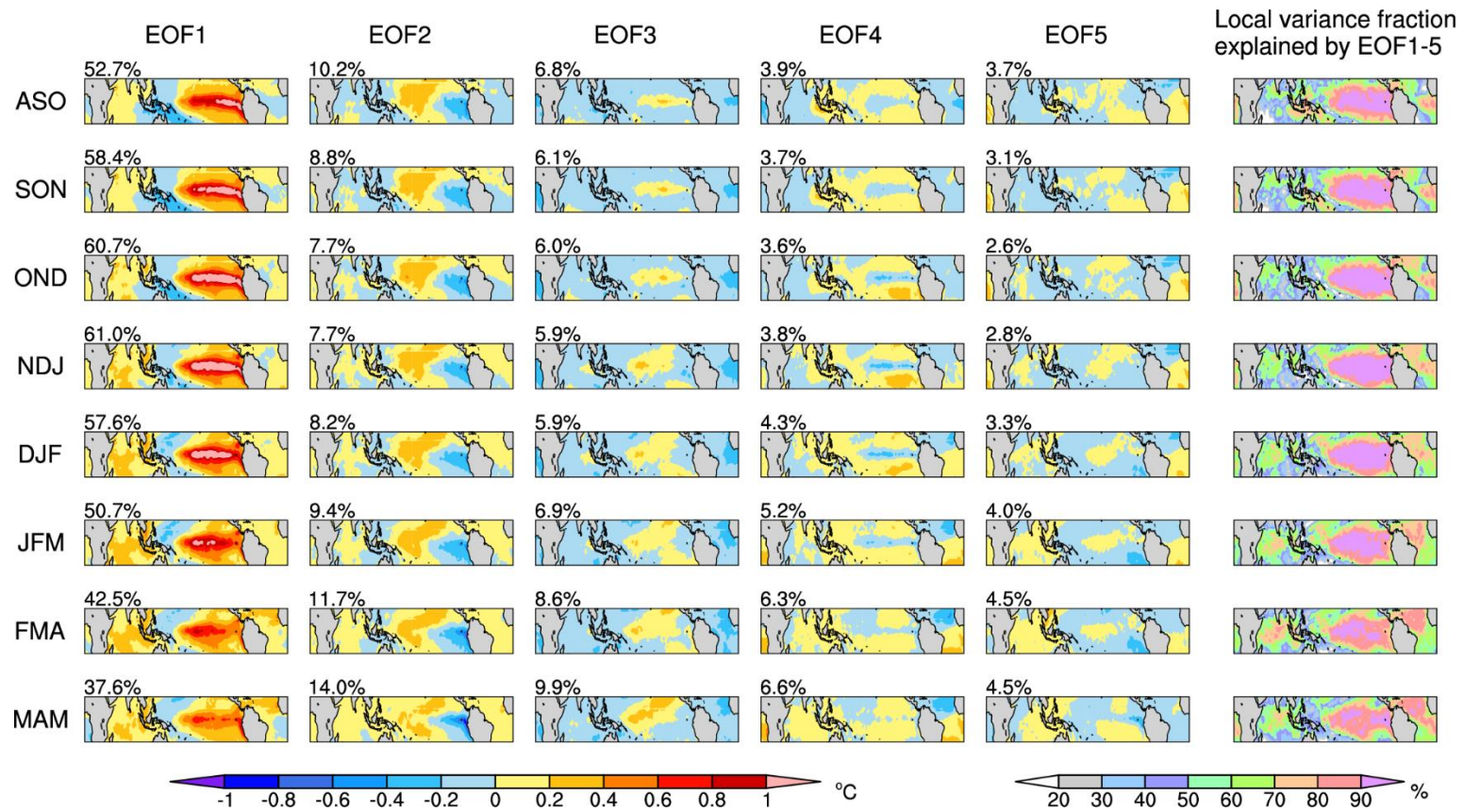


Fig. S2. (From left to right) The first to fifth EOFs of three month-mean SST over 20°S–20°N (left color bar) and local variance fraction explained by these five EOFs (right color bar) based on HadISST (1958–2021).

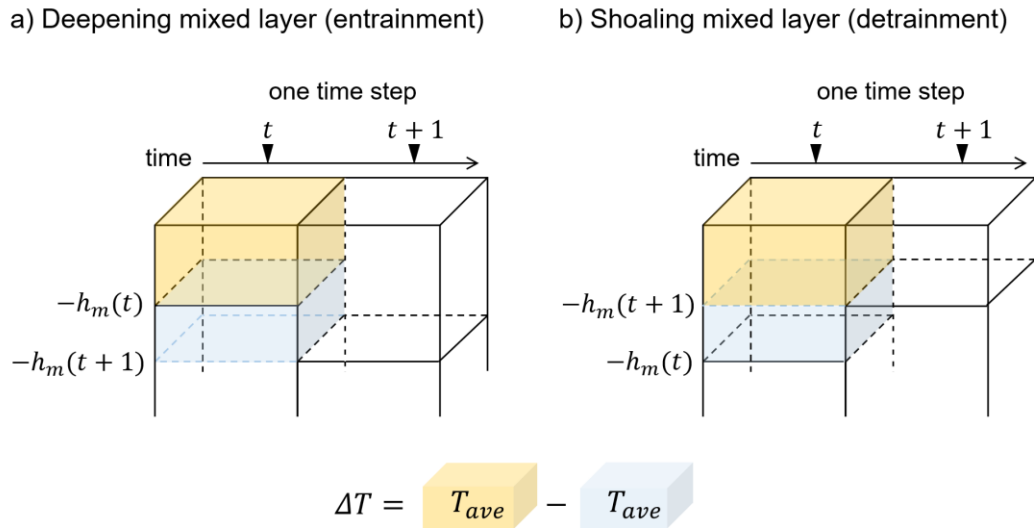


Fig. S3. Schematic of how to determine  $\Delta T$  in the formulation of the mixed-layer heat budget in the cases of (a) deepening and (b) shoaling mixed layer, based on Kim et al. (2006).

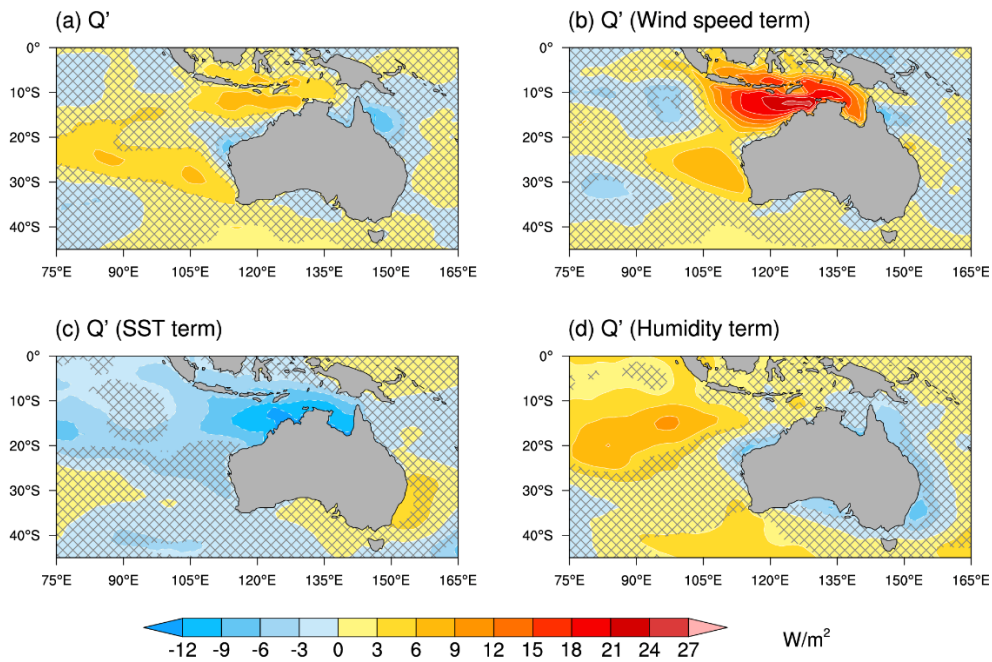


Fig. S4. (a) JF-mean surface LHF anomalies regressed onto the AUSM index. (b–d) Same as in (a) but for individual contributions from anomalies in (b) surface wind speed, (c) SST and (d) surface specific humidity, based on JRA-55 (1958–2021). Areas with significance below the 95% confidence level are hatched. See Sekizawa et al. (2018) for detail.

## MSE budget for JF anomalies

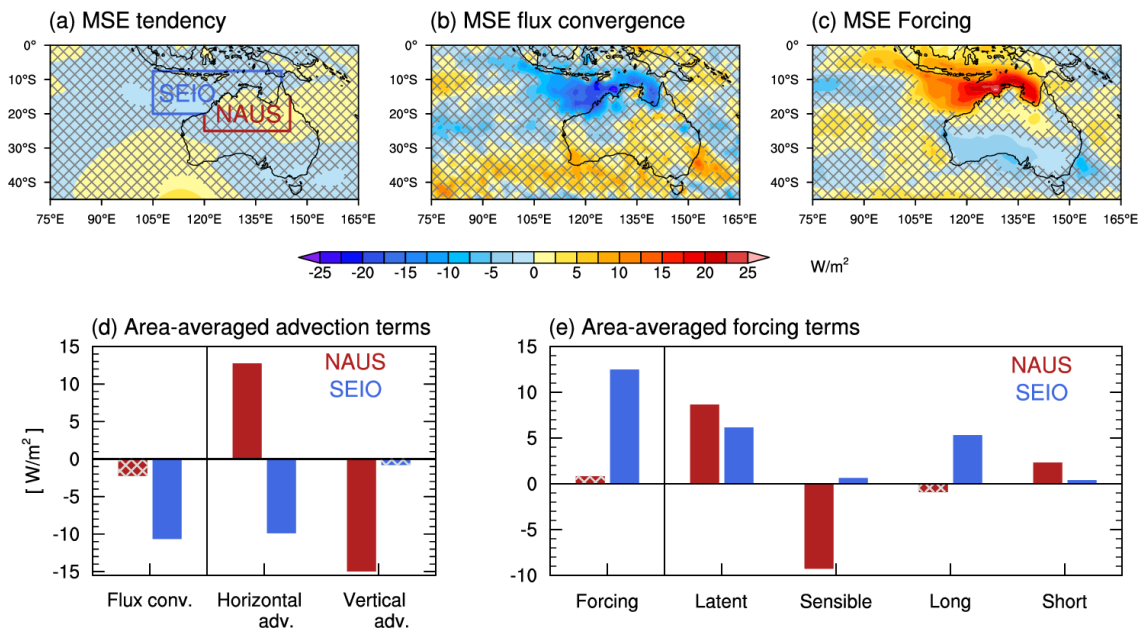


Fig. S5. Same as in Fig. 6, but based on ERA5 (1980–2021).